J Sci Comput (2013) 55:92–124
DOI 10.1007/s10915-012-9624-5

Simulation of Dynamic Earthquake Ruptures in Complex Geometries Using High-Order Finite Difference Methods

Jeremy E. Kozdon · Eric M. Dunham · Jan Nordström

Received: 15 September 2011 / Revised: 6 June 2012 / Accepted: 25 June 2012 /
Published online: 14 July 2012

Abstract We develop a stable and high-order accurate finite difference method for problems in earthquake rupture dynamics in complex geometries with multiple faults. The bulk material is an isotropic elastic solid cut by pre-existing fault interfaces that accommodate relative motion of the material on the two sides. The fields across the interfaces are related through friction laws which depend on the sliding velocity, tractions acting on the interface, and state variables which evolve according to ordinary differential equations involving local fields.

The method is based on summation-by-parts finite difference operators with irregular geometries handled through coordinate transforms and multi-block meshes. Boundary conditions as well as block interface conditions (whether frictional or otherwise) are enforced weakly through the simultaneous approximation term method, resulting in a provably stable discretization.

The theoretical accuracy and stability results are confirmed with the method of manufactured solutions. The practical benefits of the new methodology are illustrated in a simulation of a subduction zone megathrust earthquake, a challenging application problem involving complex free-surface topography, nonplanar faults, and varying material properties.

Keywords High-order finite difference · Nonlinear boundary conditions · Simultaneous approximation term method · Elastodynamics · Summation-by-parts · Friction · Wave propagation · Multi-block · Coordinate transforms · Weak boundary conditions

J.E. Kozdon (✉)
Department of Geophysics, Stanford University, Stanford, CA, USA
e-mail: jkozdon@stanford.edu

E.M. Dunham
Department of Geophysics and Institute for Computational and Mathematical Engineering, Stanford University, Stanford, CA, USA

J. Nordström
Department of Mathematics, Linköping University, Linköping, Sweden

1 Introduction

In this paper we develop a numerical method that can be applied to problems of propagating shear ruptures, particularly those arising in earthquake rupture dynamics. The rupture problem couples seismic wave propagation and frictional sliding on faults, and is thus influenced by both fault and surrounding material response. Over the temporal and spatial scales of interest in rupture dynamics, the rock response can be approximated as linear elastic (though more complex models can be considered which account for inelastic deformation) and the fault as an infinitesimally thin frictional interface.

As the material on one side of the fault is displaced with respect to the other, jump conditions relate stress and particle velocity on the two sides of the fault. The tangential displacement discontinuity across the interface is referred to as slip. The jump conditions arise from force balance considerations and constitutive laws for evolving fault strength (i.e., friction laws). Friction laws used in rupture dynamics, which are described in more detail below, depend not only on the current slip velocity and tractions acting on the fault but also on, for instance, the history of sliding, frictional heat generation, and transport of heat and pore fluids in the fault zone. The latter processes are parameterized in terms of state variables that obey differential evolution equations which are distinct from the governing equations of the elastic medium.

Earthquake simulations, and other frictional contact problems, are inherently interface driven. Hence numerical errors and instabilities arising from the treatment of the frictional interfaces can destroy the accuracy of the solution, preventing reliable ground motion predictions that are critical for seismic hazard assessment.

The method developed in this paper uses high-order finite difference methods with weak enforcement of interface and boundary conditions. In order to handle complex geometries, multi-block grids are used along with a coordinate transform formulation. The developed method is provably stable, regardless of mesh skewness, and can be used with quite general frictional formulations.

1.1 Previous Work on Seismic Wave Propagation and Dynamic Rupture Modeling

The boundary integral equation method (BIEM) has been quite popular for crack and rupture propagation problems [4, 5, 12, 13, 15, 21, 25, 35, 45, 51]. BIEM reduces the problem to solving only for the solution along the fault, with the material response entering through convolutions over the past history of slip or tractions on the fault. The main computational cost is associated with the convolutions. At least in present formulations, BIEM is limited to faults in a linear elastic medium with uniform material properties.

Finite element methods (FEM) overcome some of these computational challenges, and have been successfully applied to rupture problems [1, 36, 43, 48]. In contrast to BIEM, the entire volume is discretized, not just the faults. The meshes for FEM can be quite general and typically lower order elements with linear basis functions are used. Traditional FEM discretizations of the elastic wave equation result in nondiagonal mass matrices. Solving the resulting linear system can be avoided by lumping the mass matrix. This makes the spatial difference operator rank-deficient, leading to nonphysical oscillations (hourglass modes) that must be damped. To address this, the use of certain high-order methods, such as spectral element methods [2, 19, 26], which have diagonal mass matrices due to the choice of basis functions and quadrature points, and discontinuous Galerkin methods [16, 50], which have block-diagonal mass matrices, are gaining in popularity.

Finite difference methods, especially those on staggered grids, are also commonly used [3, 14, 15, 37, 42, 43]. These methods are very efficient for wave propagation, but proving

stability is difficult with nonlinear friction laws [56]. Additionally, staggered grid methods have difficulty handling complex geometries. A notable exception is the approach of Cruz-Atienza and Virieux [11] for nonplanar faults.

Within seismic wave propagation there has been work on the use of unstaggered grids for the first and second order form of the equations of elasticity [8, 44, 62]. Coordinate transforms have been applied to both forms of the equations to handle complex geometries [6, 20, 61].

1.2 Approach and Outline of the Paper

In our previous paper [30] we developed a strictly stable numerical method for two dimensional antiplane shear problems with nonlinear friction laws depending only on slip velocity and shear stress. That study was limited to flat faults and regular (Cartesian) meshes. Here, we extend the method to tensor elasticity in irregularly shaped domains through the use of coordinate transforms and multi-block grids. Additionally, we introduce state dependence to the friction law through the rate-and-state formalism; more details on this are given in Sect. 3.

The remainder of the paper is organized as follows. In Sect. 2 we outline the governing equations and the general computational framework. This section is designed to give the reader a roadmap for the paper, providing a concise summary of the details necessary to understand and implement the method. Section 3 presents the specific form of the boundary and interface conditions used in this work. Energy estimates for the continuous and discrete problems are derived in Sect. 4, thus proving that the method presented in Sect. 2 is stable.

These theoretical results are confirmed in Sect. 5 through two test problems. First the method of manufactured solutions is used to show that the method converges at the expected rate of accuracy on a highly skewed mesh. Next we test the practical benefits of the method by simulating a subduction zone megathrust earthquake. This simulation requires highly skewed meshes, complex free-surface topography, a nonplanar fault, and material blocks with differing physical properties. Conclusions are drawn in Sect. 6.

2 Form of the Governing Equations and Computational Approach

In this paper we consider a 2-D, isotropic elastic medium. Complex geometries are handled through the use of coordinate transforms and multi-block grids. The full computational domain is decomposed into curvilinear quadrilateral blocks. To each of the blocks coordinate transforms are applied so that the computational domain is regular (rectangular). It is in this regular domain that the high-order finite differences are applied. In the decomposition, fault and material interfaces (discontinuous changes in material properties) are mapped to block edges.

2.1 Governing Equations

We partition the computational domain $\Omega \subset \mathbb{R}^2$ into a set of disjoint, curvilinear quadrilateral blocks $\Omega^{(l)} \subset \Omega$ (see Fig. 1). The edges of the blocks can either be outer boundaries or internal interfaces. As will be seen, at the block level these can be treated identically in the discretization even though interface and boundary conditions are of a different form. Therefore we refer to boundary and interface conditions generically as edge conditions. Since the structure of the scheme does not depend on the specifics of the boundary and interface conditions, a full discussion of these is delayed until Sect. 3.

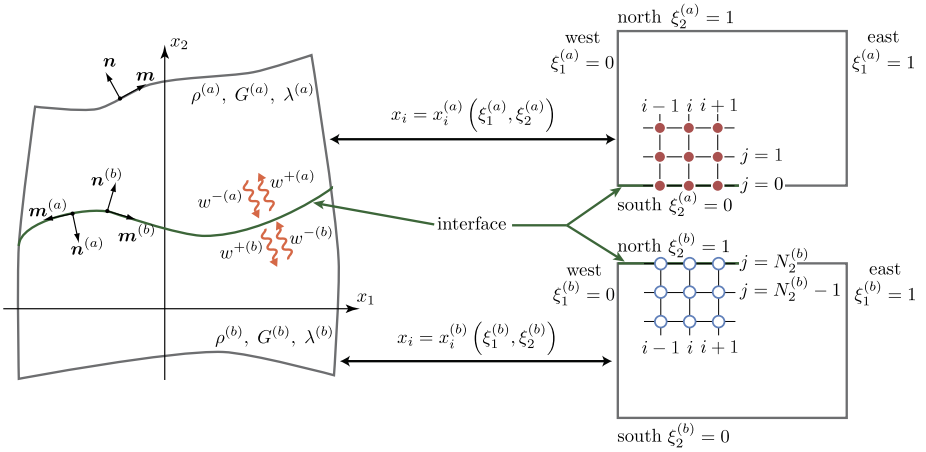

Fig. 1 Example of the coordinate transforms and multiblock decomposition. Two blocks, labeled (a) and (b), are shown with an interface between them. In this example, the interface is mapped to the south edge of block (a) ($\xi_2^{(a)}=0$) and the north edge of block (b) ($\xi_2^{(b)}=1$). As shown, the material properties in each block can be different and, apart from matching at the interface, each block has an independent coordinate transform. The unit normal $\mathbf{n}$ on each edge is outward pointing and the orthogonal unit vector $\mathbf{m}$ is defined such that $\mathbf{m}\times\mathbf{n}=\hat{\mathbf{z}}$. The variables $w^{+(a)}$ and $w^{+(b)}$ denote the characteristic variables propagating into blocks (a) and (b), respectively, and the characteristic variables $w^{-(a)}$ and $w^{-(b)}$ are those propagating out of the blocks

Within each block, the particle velocities v_i and the components of the stress tensor σ_{ij} are governed by momentum conservation and Hooke's law:

$$\rho\frac{\partial v_i}{\partial t}=\frac{\partial \sigma_{ij}}{\partial x_j}, \tag{1}$$

$$\frac{\partial \sigma_{ij}}{\partial t}=\lambda\delta_{ij}\frac{\partial v_k}{\partial x_k}+G\left(\frac{\partial v_i}{\partial x_j}+\frac{\partial v_j}{\partial x_i}\right), \tag{2}$$

where here, as in subsequent equations, Roman subscripts take values 1, 2, 3 and summation is implied over repeated Roman subscript indices. Here ρ is the density, G is the shear modulus, λ is Lamé's first parameter, and δ_{ij} is the Kronecker delta. In this paper we assume that material properties ρ, λ, and G are constant within each block, but can vary between blocks, i.e., the material properties are piecewise constant. Due to conservation of angular momentum the stress tensor is symmetric: $\sigma_{ij}=\sigma_{ji}$. Thus, governing equations (1) and (2) represent nine equations for the nine unknowns (six components of stress and three particle velocities).

Given a block $\Omega^{(l)}$ we transform to a regular domain $\widetilde{\Omega}^{(l)}=[0,1]\times[0,1]$ (see Fig. 1) using the transforms $x_1^{(l)}=x_1^{(l)}(\xi_1^{(l)},\xi_2^{(l)})$ and $x_2^{(l)}=x_2^{(l)}(\xi_1^{(l)},\xi_2^{(l)})$; we assume that this transform is invertible so that $\xi_1^{(l)}=\xi_1^{(l)}(x_1^{(l)},x_2^{(l)})$ and $\xi_2^{(l)}=\xi_2^{(l)}(x_1^{(l)},x_2^{(l)})$ also exist. Across block interfaces we require the transform to be conforming, e.g., in Fig. 1 $x_i^{(a)}(\xi_1,0)=x_i^{(b)}(\xi_1,1)$, but no other smoothness constraints are imposed across the interfaces. The Jacobian determinant is then

$$J=\frac{\partial x_1}{\partial \xi_1}\frac{\partial x_2}{\partial \xi_2}-\frac{\partial x_1}{\partial \xi_2}\frac{\partial x_2}{\partial \xi_1}, \tag{3}$$

where here, as in the remainder of the paper, we drop the superscript (l) when considering a single block unless it is necessary for clarity. The coordinate transform and Jacobian determinant give rise to the metric relations

$$J\frac{\partial \xi_1}{\partial x_1} = \frac{\partial x_2}{\partial \xi_2}, \qquad J\frac{\partial \xi_1}{\partial x_2} = -\frac{\partial x_1}{\partial \xi_2}, \qquad J\frac{\partial \xi_2}{\partial x_2} = \frac{\partial x_1}{\partial \xi_1}, \qquad J\frac{\partial \xi_2}{\partial x_1} = -\frac{\partial x_2}{\partial \xi_1}. \tag{4}$$

Using the metric relations, conservation of momentum (1) and Hooke's law (2) can be expressed in the transformed coordinate system as

$$\rho J\frac{\partial v_i}{\partial t} = \gamma\frac{\partial}{\partial \xi_\alpha}\left(J\frac{\partial \xi_\alpha}{\partial x_j}\sigma_{ij}\right) + (1-\gamma)J\frac{\partial \xi_\alpha}{\partial x_j}\frac{\partial \sigma_{ij}}{\partial \xi_\alpha}, \tag{5}$$

$$\begin{aligned} J\frac{\partial \sigma_{ij}}{\partial t} &= \gamma\left[\lambda\delta_{ij}\frac{\partial}{\partial \xi_\alpha}\left(J\frac{\partial \xi_\alpha}{\partial x_k}v_k\right) + G\frac{\partial}{\partial \xi_\alpha}\left(J\frac{\partial \xi_\alpha}{\partial x_j}v_i + J\frac{\partial \xi_\alpha}{\partial x_i}v_j\right)\right] \\ &\quad + (1-\gamma)\left[\lambda\delta_{ij}J\frac{\partial \xi_\alpha}{\partial x_k}\frac{\partial v_k}{\partial \xi_\alpha} + G\left(J\frac{\partial \xi_\alpha}{\partial x_j}\frac{\partial v_i}{\partial \xi_\alpha} + J\frac{\partial \xi_\alpha}{\partial x_i}\frac{\partial v_j}{\partial \xi_\alpha}\right)\right], \end{aligned} \tag{6}$$

where here, as in subsequent equations, summation is implied over 1 and 2 for repeated Greek subscript indices. The parameter γ can take any value in the continuous problem. It is common to set $\gamma = 1$ so that in the constant coefficient case the equations can be written in conservation form. Unfortunately this introduces an energy instability in the discretized equations [47], which is particularly pronounced on highly skewed grids with long time integration. Instead, we will show that with $\gamma = 1/2$ a provably stable method can be developed regardless of mesh skewness [46].

To fully specify the problem the edge conditions are required. The form of these is given in Sect. 3, but in order to present the method a few definitions are required. Consider the single edge of a block. We define $\mathbf{n} = [n_1, n_2, 0]^T$ to be the outward pointing unit normal to the block edge. Since we are considering a 2-D domain, the unit vector $\hat{\mathbf{z}} = [0, 0, 1]^T$ is orthogonal to $\mathbf{n}$ and we define $\mathbf{m} = \mathbf{n} \times \hat{\mathbf{z}} = [n_2, -n_1, 0]^T$ to be the second orthogonal coordinate direction (see Fig. 1). The stress tensor and particle velocities can now be rotated into this new coordinate system, and it is in this rotated coordinate system that we apply the edge conditions. Namely, we define the rotated particle velocities

$$v_n = n_i v_i, \qquad v_m = m_i v_i, \qquad v_z = v_3, \tag{7}$$

which are the components of particle velocity normal (v_n) and orthogonal (v_m, v_z) to the edge. The components of traction acting on the interface are

$$T_i = \sigma_{ij} n_j. \tag{8}$$

The tractions can be further decomposed into the normal traction σ_n (taken to be positive in compression) as well as the two components of shear traction τ_m and τ_z, aligned with $\mathbf{m}$ and $\hat{\mathbf{z}}$, acting on the interface:

$$\sigma_n = -n_i T_i = -n_i \sigma_{ij} n_j, \qquad \tau_m = m_i T_i = m_i \sigma_{ij} n_j, \qquad \tau_z = \hat{z}_i T_i = \hat{z}_i \sigma_{ij} n_j, \tag{9}$$

$$T_i = -\sigma_n n_i + \tau_m m_i + \tau_z \hat{z}_i. \tag{10}$$

There are three additional components of stress in the new coordinate system which do not exert tractions on the interface:

$$\sigma_m = m_i \sigma_{ij} m_j, \qquad \sigma_{mz} = m_i \sigma_{ij} \hat{z}_j, \qquad \sigma_z = \hat{z}_i \sigma_{ij} \hat{z}_j = \sigma_{33}. \tag{11}$$

We now assume that edge conditions are of the form

$$g_n(T_i, v_i) = 0, \qquad g_m(T_i, v_i) = 0, \qquad g_z(T_i, v_i) = 0, \tag{12}$$

where g_n, g_m, and g_z can be linear or nonlinear functions and in the case of interface conditions will depend on the solution on both sides of the interface.

2.2 Discrete Framework

As in our previous work, we use summation-by-parts (SBP) finite difference methods [10, 33, 34, 39, 59] on an unstaggered grid. An SBP difference approximation to the first derivative has the form

$$\frac{\partial v}{\partial x} \approx \boldsymbol{H}^{-1}\boldsymbol{Q}\mathbf{v}, \tag{13}$$

where $\boldsymbol{H}$ is a symmetric positive definite matrix, $\boldsymbol{Q}$ is an almost skew-symmetric matrix with $\boldsymbol{Q}^T + \boldsymbol{Q} = \boldsymbol{B} = \mathbf{diag}[-1, 0, \ldots, 0, 1]$, and the vector $\mathbf{v} = [v_0, v_1, \ldots, v_N]^T$ is the grid data. These are called SBP methods because they mimic integration-by-parts properties of the continuous problem. Defining the continuous and discrete inner products

$$(u, v) = \int_a^b u(x)v(x)dx \quad \text{and} \quad (\mathbf{u}, \mathbf{v})_h = \mathbf{u}^T\boldsymbol{H}\mathbf{v}, \tag{14}$$

this becomes clear since

$$\left(v, \frac{dv}{dx}\right) = \int_a^b v\frac{dv}{dx}dx = \frac{1}{2}\big[v(b)^2 - v(a)^2\big], \tag{15}$$

$$\big(\mathbf{v}, \boldsymbol{H}^{-1}\boldsymbol{Q}\mathbf{v}\big)_h = \mathbf{v}^T\boldsymbol{Q}\mathbf{v} = \frac{1}{2}\mathbf{v}^T\big(\boldsymbol{Q} + \boldsymbol{Q}^T\big)\mathbf{v} = \frac{1}{2}\big(v_N^2 - v_0^2\big). \tag{16}$$

SBP operators are standard central difference operators, having orders $q = 2, 4, 6, 8, \ldots$ in the interior, that become one-sided operators near boundaries in a manner that ensures the SBP property. The boundary order of accuracy r is typically lower than the interior accuracy q and hence the global accuracy is $p = r + 1$ [22, 60]. In this work we only consider diagonal norm (diagonal $\boldsymbol{H}$) operators which have interior accuracy $q = 2s$ ($s = 1, 2, \ldots$), boundary accuracy $r = s$, and global accuracy $p = s + 1$. There are SBP operators that have boundary accuracy $r = 2s - 1$ and global accuracy $p = 2s$, but using these makes stability proofs difficult for problems with variable coefficients, coordinate transforms, and nonlinear boundary/interface conditions [30, 46, 47, 49].

Each block $\widetilde{\Omega}^{(l)}$ is discretized using an $N_1^{(l)} \times N_2^{(l)}$ grid; note that each block can have a different number of grid cells, but the grids must conform at the block interfaces, i.e., have the same number of collocated grid points on both sides of the interface. Let $\mathbf{v}_i$ and $\boldsymbol{\sigma}_{ij}$ be the particle velocities and stresses on the grid stacked as vectors:

$$\mathbf{v}_i = \big[(v_i)_{00}, (v_i)_{01}, \ldots, (v_i)_{N_1N_2}\big]^T, \tag{17}$$

$$\boldsymbol{\sigma}_{ij} = \big[(\sigma_{ij})_{00}, (\sigma_{ij})_{01}, \ldots, (\sigma_{ij})_{N_1N_2}\big]^T. \tag{18}$$

The transformed governing equations (5) and (6) are then discretized in space using dimension-by-dimension application of the 1-D difference operators,

$$\rho \boldsymbol{J} \frac{\partial \mathbf{v}_i}{\partial t} = \gamma \bar{\boldsymbol{D}}_\alpha \left(\boldsymbol{J} \frac{\partial \boldsymbol{\xi}_\alpha}{\partial x_j} \boldsymbol{\sigma}_{ij} \right) + (1-\gamma) \boldsymbol{J} \frac{\partial \boldsymbol{\xi}_\alpha}{\partial x_j} \bar{\boldsymbol{D}}_\alpha \boldsymbol{\sigma}_{ij} + \rho \boldsymbol{\mathcal{P}}_i^N + \rho \boldsymbol{\mathcal{P}}_i^S + \rho \boldsymbol{\mathcal{P}}_i^E + \rho \boldsymbol{\mathcal{P}}_i^W, \tag{19}$$

$$\boldsymbol{J} \frac{\partial \boldsymbol{\sigma}_{ij}}{\partial t} = \gamma \left\{ \lambda \delta_{ij} \bar{\boldsymbol{D}}_\alpha \left(\boldsymbol{J} \frac{\partial \boldsymbol{\xi}_\alpha}{\partial x_k} \mathbf{v}_k \right) + G \bar{\boldsymbol{D}}_\alpha \left(\boldsymbol{J} \frac{\partial \boldsymbol{\xi}_\alpha}{\partial x_j} \mathbf{v}_i + \boldsymbol{J} \frac{\partial \boldsymbol{\xi}_\alpha}{\partial x_i} \mathbf{v}_j \right) \right\} + (1-\gamma) \left[\lambda \delta_{ij} \boldsymbol{J} \frac{\partial \boldsymbol{\xi}_\alpha}{\partial x_k} \bar{\boldsymbol{D}}_\alpha \mathbf{v}_k + G \left(\boldsymbol{J} \frac{\partial \boldsymbol{\xi}_\alpha}{\partial x_j} \bar{\boldsymbol{D}}_\alpha \mathbf{v}_i + \boldsymbol{J} \frac{\partial \boldsymbol{\xi}_\alpha}{\partial x_i} \bar{\boldsymbol{D}}_\alpha \mathbf{v}_j \right) \right] + \boldsymbol{\mathcal{P}}_{ij}^N + \boldsymbol{\mathcal{P}}_{ij}^S + \boldsymbol{\mathcal{P}}_{ij}^E + \boldsymbol{\mathcal{P}}_{ij}^W, \tag{20}$$

where the matrices $\boldsymbol{J}$ and $\partial \boldsymbol{\xi}_\alpha / \partial x_i$ are diagonal matrices with elements along the diagonal ordered in the same manner as $\mathbf{v}_i$ and $\boldsymbol{\sigma}_{ij}$. The difference operators are defined as

$$\bar{\boldsymbol{D}}_1 = \boldsymbol{D}_1 \otimes \boldsymbol{I}_{N_2}, \qquad \bar{\boldsymbol{D}}_2 = \boldsymbol{I}_{N_1} \otimes \boldsymbol{D}_2, \tag{21}$$

with $\boldsymbol{D}_\alpha$ being the 1-D SBP difference operators, $\boldsymbol{I}_{N_\alpha}$ being the $N_\alpha \times N_\alpha$ identity matrix, and $\otimes$ representing the Kronecker product of two matrices.

Weak enforcement of the edge conditions is captured via the penalty terms $\boldsymbol{\mathcal{P}}_i$ and $\boldsymbol{\mathcal{P}}_{ij}$ where the superscripts refer to each of the block edges: N refers to the "north" edge $\xi_2 = 1$, S to the "south" edge $\xi_2 = 0$, E to the "east" edge $\xi_1 = 1$, and W to the "west" edge $\xi_1 = 0$; see Fig. 1. Since we consider only the diagonal norm SBP operators, the penalty terms only act on grid points along the block edges. Thus, the penalty terms take the form of vectors which are zero except for the grid points on the edge to which they refer, e.g., along the west edge they are of the form

$$\boldsymbol{\mathcal{P}}_i^W = \left[(\mathcal{P}_i^W)_{00}, \ldots, (\mathcal{P}_i^W)_{0N_2}, 0, \ldots, 0 \right]^T, \tag{22}$$

$$\boldsymbol{\mathcal{P}}_{ij}^W = \left[(\mathcal{P}_{ij}^W)_{00}, \ldots, (\mathcal{P}_{ij}^W)_{0N_2}, 0, \ldots, 0 \right]^T, \tag{23}$$

and similarly for the other edges.

In order to state the penalty terms we consider a single grid point on one of the block edges; for clarity in this discussion we drop the subscripts denoting grid index. From the grid data we define the *hat variables*

$$\hat{v}_n, \ \hat{v}_m, \ \hat{v}_z, \ \hat{\sigma}_n, \ \hat{\sigma}_m, \ \hat{\sigma}_{mz}, \ \hat{\sigma}_z, \ \hat{\tau}_m, \ \hat{\tau}_z, \tag{24}$$

which satisfy the edge conditions (12), and are dependent on the grid solution at the edge; the specific form of these is given in Sect. 3 and it will be shown that these hat variables are defined in a manner that only modifies the three characteristic variables propagating into the block. These hat variables are written in terms of the edge local coordinate system; they can of course be rewritten in terms of the global coordinate system using the inverse relations to (7), (9), and (11):

$$\hat{v}_i = n_i \hat{v}_n + m_i \hat{v}_m + \hat{z}_i \hat{v}_z, \tag{25}$$

$$\hat{\sigma}_{ij} = -n_i \hat{\sigma}_n n_j + m_i \hat{\sigma}_m m_j + \hat{z}_i \hat{\sigma}_z \hat{z}_j + m_i \hat{\sigma}_{mz} \hat{z}_j + m_i \hat{\tau}_m n_j + \hat{z}_i \hat{\tau}_z n_j. \tag{26}$$

The terms arising in the penalty vector then take the general form

$$\begin{bmatrix} \mathcal{P}_1 \\ \mathcal{P}_2 \\ \mathcal{P}_3 \\ \mathcal{P}_{11} \\ \mathcal{P}_{12} \\ \mathcal{P}_{13} \\ \mathcal{P}_{22} \\ \mathcal{P}_{23} \\ \mathcal{P}_{33} \end{bmatrix} = \begin{bmatrix} \boldsymbol{\Sigma}_1^T \\ \boldsymbol{\Sigma}_2^T \\ \boldsymbol{\Sigma}_3^T \\ \boldsymbol{\Sigma}_{11}^T \\ \boldsymbol{\Sigma}_{12}^T \\ \boldsymbol{\Sigma}_{13}^T \\ \boldsymbol{\Sigma}_{22}^T \\ \boldsymbol{\Sigma}_{23}^T \\ \boldsymbol{\Sigma}_{33}^T \end{bmatrix} \left(\begin{bmatrix} v_1 \\ v_2 \\ v_3 \\ \sigma_{11} \\ \sigma_{12} \\ \sigma_{13} \\ \sigma_{22} \\ \sigma_{23} \\ \sigma_{33} \end{bmatrix} - \begin{bmatrix} \hat{v}_1 \\ \hat{v}_2 \\ \hat{v}_3 \\ \hat{\sigma}_{11} \\ \hat{\sigma}_{12} \\ \hat{\sigma}_{13} \\ \hat{\sigma}_{22} \\ \hat{\sigma}_{23} \\ \hat{\sigma}_{33} \end{bmatrix} \right) = \boldsymbol{\Sigma}(\mathbf{q} - \hat{\mathbf{q}}), \tag{27}$$

where $\boldsymbol{\Sigma}$ is the penalty matrix for the grid point under consideration and is chosen such that the scheme is stable. The form above is quite general, but obscures the simplicity of the method. Thus, we now write down the specific form that the penalty terms take after appropriate choice of $\boldsymbol{\Sigma}$ (see Kozdon et al. [30] for details):

$$\begin{aligned} \mathcal{P}_i &= \boldsymbol{\Sigma}_i^T(\mathbf{q} - \hat{\mathbf{q}}) \\ &= -\frac{1}{T_p} n_i (v_n - \hat{v}_n) - \frac{1}{T_s} m_i (v_m - \hat{v}_m) - \frac{1}{T_s} \hat{z}_i (v_z - \hat{v}_z), \end{aligned} \tag{28}$$

$$\begin{aligned} \mathcal{P}_{ij} &= \boldsymbol{\Sigma}_{ij}^T(\mathbf{q} - \hat{\mathbf{q}}) \\ &= \frac{1}{T_p} n_i n_j (\sigma_n - \hat{\sigma}_n) - \frac{1}{T_p} m_i m_j (\sigma_m - \hat{\sigma}_m) - \frac{1}{T_p} \hat{z}_i \hat{z}_j (\sigma_z - \hat{\sigma}_z) \\ &\quad - \frac{1}{T_s} (n_i m_j + n_j m_i)(\tau_m - \hat{\tau}_m) - \frac{1}{T_s} (n_i \hat{z}_j + n_j \hat{z}_i)(\tau_z - \hat{\tau}_z), \end{aligned} \tag{29}$$

where T_s and T_p will be chosen such that the method is provably stable; the lack of minus sign on σ_n is due to the sign convention that σ_n is positive in compression. Here v_n, v_m, v_z, σ_n, σ_m, σ_z, τ_m, and τ_z correspond to the grid data rotated into the edge local coordinate system; see (7), (9), and (11). The possible schemes represented by (28) and (29) are a subset of all possible schemes represented by (27); see Kozdon et al. [30] for a more detailed discussion.

The penalty terms written in the form of (28) and (29) can be interpreted physically as relaxation of the grid data v_i and σ_{ij} towards values which satisfy the edge conditions $\hat{v}_i$ and $\hat{\sigma}_{ij}$ (the hat variables) over the relaxation times T_p and T_s. As will be seen in Sect. 4.2, these relaxation times scale as $T_p \sim h/c_p$ and $T_s \sim h/c_s$ with c_p and c_s being the P-wave and S-wave speeds, respectively, and h being the grid spacing. Since the relaxation times scale with the grid spacing h the relaxation times go to zero under grid refinement and the edge condition is enforced exactly. The vectors $\mathbf{n}$, $\mathbf{m}$, and $\hat{\mathbf{z}}$ arise because the stresses and velocities must be rotated into a coordinate system that is aligned with the edge.

For practical implementation of the method, the formulation (28) and (29) is extremely convenient for two reasons. First, as will be seen in Sect. 3, the edge condition and hat variables are easily stated in terms of the local rotated coordinates. Second, and perhaps more importantly, the treatment of all edges is the same regardless of whether the edge is a boundary, locked interface, or frictional fault. That is, T_p and T_s are the same for both external boundaries and interfaces and are independent of the specific edge condition. This

greatly simplifies code development by increasing modularity, allowing for a single set of routines for all blocks; of course different subroutines are required to set the hat variables for each edge condition.

3 Boundary and Interface Conditions

Here we give the specific form for the edge conditions (12). As noted above, the edges of blocks are either outer boundaries or interfaces with other blocks. Since the governing equations (1) and (2) are hyperbolic, the number of edge conditions can be derived from a characteristic decomposition in the local, rotated coordinate system [31]. There are two characteristic variables associated with the P-waves and four characteristic variables associated with the S-waves; additionally there are three characteristic variables associated with zero speed waves.

If we consider the outward normal $\mathbf{n}$ to a single block of the domain, there are three characteristic variables propagating into and three propagating out of the block. The two characteristic variables associated with the P-waves, travelling at velocity $c_p = \sqrt{(\lambda + 2G)/\rho}$ in the directions $\mp\mathbf{n}$, are

$$w_n^{\pm} = -\sigma_n \pm Z_p v_n, \tag{30}$$

where $Z_p = \rho c_p$ is the dilatational impedance of the material. Similarly, the four characteristic variables associated with the S-waves, propagating in the $\mp\mathbf{n}$ directions with velocity $c_s = \sqrt{G/\rho}$, are

$$w_m^{\pm} = \tau_m \pm Z_s v_m, \qquad w_z^{\pm} = \tau_z \pm Z_s v_z, \tag{31}$$

where $Z_s = \rho c_s$ is the shear impedance of the material. The variable $w_m^{\pm}$ is polarized in the $\mathbf{m}$ direction and $w_z^{\pm}$ in the $\hat{\mathbf{z}}$ direction. If $\hat{\mathbf{z}}$ were the vertical direction, i.e., normal to Earth's surface, then w_m and w_z would be associated with the SH and SV polarized S-waves, respectively. It is worth highlighting that $w_n^{\pm}$ transmits normal tractions and velocities to the edges, and $w_m^{\pm}$ and $w_z^{\pm}$ transmit shear tractions and edge parallel velocities. To simplify the notation, we define the vectors

$$\mathbf{w}^{\pm} = \begin{bmatrix} w_n^{\pm} \\ w_m^{\pm} \\ w_z^{\pm} \end{bmatrix}. \tag{32}$$

With the definition that $\mathbf{n}$ is the outward pointing normal, $\mathbf{w}^+$ corresponds to the characteristic variables propagating into the block and $\mathbf{w}^-$ to those propagating out of the block; see Fig. 1. As mentioned above, there are additionally three zero speed waves:

$$\mathring{w}_m = \sigma_m + \left(1 - 2\frac{c_s^2}{c_p^2}\right)\sigma_n, \qquad \mathring{w}_z = \sigma_z + \left(1 - 2\frac{c_s^2}{c_p^2}\right)\sigma_n, \qquad \mathring{w}_{mz} = \sigma_{mz}. \tag{33}$$

3.1 Outer Boundary Conditions

This characteristic analysis implies that we need three edge conditions relating the characteristics propagating into the block to the characteristics propagating out of the block. If the edges are outer boundaries, we take these to be the simple linear expressions

$$\mathbf{w}^+ = R\mathbf{w}^-, \tag{34}$$

where $-1 \leq R \leq 1$ is a reflection coefficient. Of course, more general boundary conditions are possible, but this suffices for this paper where our primary interest is the treatment of complex geometries and nonlinear interface conditions. Two important boundary conditions are the free surface boundary condition $T_i = 0$ which results with $R = -1$, and the absorbing boundary condition when $R = 0$. In the case of the absorbing boundary conditions, more effective nonreflecting boundary conditions are possible (e.g., [7, 24]), though we do not consider these in this work.

3.2 Locked (Non-frictional) Interface Conditions

In the case of interfaces, say between blocks $\Omega^{(a)}$ and $\Omega^{(b)}$, the interface conditions take the general form:

$$\mathbf{w}^{+(a)} = \mathcal{W}^{+(a)}\left(\mathbf{w}^{-(a)}, \mathbf{w}^{-(b)}\right), \tag{35}$$

that is the characteristic variables propagating into the block are a (potentially) nonlinear combination of the characteristic variables propagating out of the block (and into the interface). In this work we will consider two different types of interfaces, leading to two different expressions for $\mathcal{W}^{+(a)}$. The simplest case is when the interface between blocks $\Omega^{(a)}$ and $\Omega^{(b)}$ is not a frictional fault, that is when the interface has been introduced to handle a change in material properties or for purely computational reasons. We call this a *locked interface*. In the case of the locked interface $\mathcal{W}^{+(a)}$ is a linear function. Though it is possible to state the explicit form of this linear relation, it is easier to state the interface conditions in terms of the physical variables. Force balance requires that across the interface the tractions must be equal and opposite, $T_i^{(a)} = -T_i^{(b)}$, or equivalently given our definitions of the outward normal and orthogonal vectors

$$\sigma_n^{(a)} = \sigma_n^{(b)}, \qquad \tau_m^{(a)} = \tau_m^{(b)}, \qquad \tau_z^{(a)} = -\tau_z^{(b)}. \tag{36}$$

Additionally, since the interface is locked this means that the velocities are continuous across the interface so that

$$v_n^{(a)} = -v_n^{(b)}, \qquad v_m^{(a)} = -v_m^{(b)}, \qquad v_z^{(a)} = v_z^{(b)}. \tag{37}$$

This represents six conditions for the interface, which is the correct number since each side requires three expressions; it is straightforward to show that these can be written in the characteristic form of $\mathcal{W}^{+(a)}$ and $\mathcal{W}^{+(b)}$. The difference in sign of the z component in (36) and (37) is due to the fact that $\hat{\mathbf{z}}^{(a)} = \hat{\mathbf{z}}^{(b)}$ whereas $\mathbf{n}^{(a)} = -\mathbf{n}^{(b)}$ and $\mathbf{m}^{(a)} = -\mathbf{m}^{(b)}$.

3.3 Frictional Interface Conditions

The more interesting case is a frictional interface. As shown in the Appendix, there is no general closed form expression for $\mathcal{W}^{+(a)}$ and $\mathcal{W}^{+(b)}$ in the case of a frictional interface. Instead we will write down the friction law in the physical variables, a nonlinear relation between the velocities and the tractions, and derive a set of sufficient conditions that guarantee the existence of a unique characteristic form. As in the case of a locked interface, force balance (36) requires that the tractions be equal and opposite across the interface. We impose the physical constraint that the fault remain closed, which implies that the opening velocity be zero, or alternatively that the normal component of particle velocity be continuous across the interface,

$$v_n^{(a)} = -v_n^{(b)}. \tag{38}$$

Since the components of the fault tangential velocity are permitted to be discontinuous, we define the slip velocity vector:

$$\mathbf{V} = \begin{bmatrix} V_m \\ V_z \end{bmatrix} = \begin{bmatrix} -v_m^{(a)} - v_m^{(b)} \\ -v_z^{(a)} + v_z^{(b)} \end{bmatrix}, \tag{39}$$

where, as in the locked interface case, the difference in sign in the components is due to the definition of the fault tangential unit vectors. We denote the magnitude of the slip velocity as $V = \|\mathbf{V}\|$. The nonlinear relation between the stress and the velocity must be determined through experiments and theoretical considerations of the physics of frictional contact (though mathematical considerations can place some constraints on the form of these relations). In this work we exclusively consider friction laws of the form:

$$\boldsymbol{\tau} = \bar{\sigma}_n f(V, \psi) \frac{\mathbf{V}}{V}, \tag{40}$$

where $\bar{\sigma}_n = \max(\sigma_n, 0)$ and $\boldsymbol{\tau} = [\tau_m^{(a)}, \tau_z^{(a)}]^T$. Note we have defined the components of the shear traction vector with respect to side (a), if we were to define it with respect to (b) then $V_z = v_z^{(a)} - v_z^{(b)}$. The form of friction law (40) implies that $\boldsymbol{\tau}$ and $\mathbf{V}$ are parallel. Physically this says that the shear tractions are acting to resist fault motion. The frictional coefficient f is a nonlinear function of both the magnitude of the slip velocity V and a state variable ψ, and is defined such that $f \geq 0$. The state variable ψ is governed by an ordinary differential equation

$$\frac{d\psi}{dt} = G(V, \psi). \tag{41}$$

Specific forms for $f(V, \psi)$ and $G(V, \psi)$ will be given in Sect. 5. If $\partial f / \partial V \geq 0$ then, using the implicit function theorem along with equal and opposite tractions as well as non-opening, it is possible to show that these nonlinear interface conditions take the form of (35), i.e., a characteristic form exists although no closed form expression is known; see the Appendix for more details.

3.4 Hat Variables

In the definition of the penalty terms (28) and (29) we introduced a set of hat variables (24). Here, we are now able to define these more precisely. Let v_n, v_m, v_z, σ_n, σ_m, σ_z, τ_m, and τ_z be the solution at a grid point on the edge of a block rotated into the edge local coordinate system using the local normal vector $\mathbf{n}$ and the two orthogonal vectors $\mathbf{m}$ and $\hat{\mathbf{z}}$; see (7), (9), and (11).

With these values we can define the incoming and outgoing characteristic variables $\mathbf{w}^{\pm}$; see (30) and (31). The edge conditions give us the boundary or interface conditions in terms of the characteristic variables propagating out of the block, that is we can also define $\boldsymbol{\mathcal{W}}^+$ as the edge condition evaluated with $\mathbf{w}^-$. When the edge is an interface between two blocks (a) and (b) the edge conditions $\boldsymbol{\mathcal{W}}^{+(a)}$ and $\boldsymbol{\mathcal{W}}^{+(b)}$ are evaluated using the characteristic variables propagating out of both blocks, $\mathbf{w}^{-(a)}$ and $\mathbf{w}^{-(b)}$.

We now define the hat variables using $\mathbf{w}^-$ and $\boldsymbol{\mathcal{W}}^+$. The particle velocities are defined as

$$\hat{v}_n = \frac{1}{2Z_p}\left(w_n^+ - \mathcal{W}_n^-\right), \qquad \hat{v}_m = \frac{1}{2Z_s}\left(w_m^+ - \mathcal{W}_m^-\right), \qquad \hat{v}_z = \frac{1}{2Z_s}\left(w_z^+ - \mathcal{W}_z^-\right), \tag{42}$$

and the tractions as

$$\hat{\sigma}_n = -\frac{1}{2}\big(w_n^+ + \mathcal{W}_n^-\big), \qquad \hat{\tau}_m = \frac{1}{2}\big(w_m^+ + \mathcal{W}_m^-\big), \qquad \hat{\tau}_z = \frac{1}{2}\big(w_z^+ + \mathcal{W}_z^-\big), \tag{43}$$

along with the components of stress which do not exert tractions on the interface

$$\hat{\sigma}_m = \mathring{w}_m - \left(1 - 2\frac{c_s^2}{c_p^2}\right)\hat{\sigma}_n, \qquad \hat{\sigma}_z = \mathring{w}_z - \left(1 - 2\frac{c_s^2}{c_p^2}\right)\hat{\sigma}_n, \qquad \hat{\sigma}_{mz} = \mathring{w}_{mz}, \tag{44}$$

where $\mathring{w}_m$, $\mathring{w}_z$, and $\mathring{w}_{mz}$ are the zero speed characteristic variables (33).

One of the properties of these hat variables is that by construction they exactly satisfy the edge conditions both in terms of the characteristic variables and the physical variables. This is important when the edge is an interface between two blocks, say blocks (a) and (b). In the case of a locked interface the particle velocities are continuous with equal and opposite tractions (see (36) and (37)):

$$\hat{\sigma}_n^{(a)} = \hat{\sigma}_n^{(b)}, \qquad \hat{\tau}_m^{(a)} = \hat{\tau}_m^{(b)}, \qquad \hat{\tau}_z^{(a)} = -\hat{\tau}_z^{(b)}, \tag{45}$$

$$\hat{v}_n^{(a)} = -\hat{v}_n^{(b)}, \qquad \hat{v}_m^{(a)} = -\hat{v}_m^{(b)}, \qquad \hat{v}_z^{(a)} = \hat{v}_z^{(b)}. \tag{46}$$

Similarly, when the edge is a frictional interface, the hat variables satisfy the nonlinear friction law (40) and continuity conditions

$$\hat{\boldsymbol{\tau}} = \bar{\sigma}_n f(\hat{V}, \psi)\frac{\hat{\mathbf{V}}}{\hat{V}}, \qquad \hat{\tau}_m^{(a)} = \hat{\tau}_m^{(b)}, \qquad \hat{\tau}_z^{(a)} = -\hat{\tau}_z^{(b)}, \tag{47}$$

$$\hat{\sigma}_n^{(a)} = \hat{\sigma}_n^{(b)}, \qquad \hat{v}_n^{(a)} = -\hat{v}_n^{(b)}. \tag{48}$$

Additionally, when integrating the state variable ψ with (41) we use $\hat{V}$ and not V as defined by the grid data.

4 Energy Estimates

In order to develop an energy estimate, we need both continuous and discrete energy norms E and E_h, that is positive definite functionals of the solution. In general there are an infinite number of possibilities for this, but for the equations of linear elasticity it is convenient to choose the norm that corresponds to the physical energy in the system. Namely, we let

$$E(t) = \sum_l E^{(l)}(t), \tag{49}$$

$$\begin{aligned} E^{(l)}(t) &= \iint_{\Omega^{(l)}} \left[\frac{\rho}{2} v_i v_i + \frac{1}{4G}\sigma_{ij}\left(\sigma_{ij} - \frac{\lambda}{3\lambda + 2G}\sigma_{kk}\delta_{ij}\right)\right] dx_1 dx_2 \\ &= \iint_{\widetilde{\Omega}^{(l)}} \left[\frac{\rho}{2} v_i v_i + \frac{1}{4G}\sigma_{ij}\left(\sigma_{ij} - \frac{\lambda}{3\lambda + 2G}\sigma_{kk}\delta_{ij}\right)\right] J\, d\xi_1 d\xi_2, \end{aligned} \tag{50}$$

where $E^{(l)}(t)$ corresponds to the total mechanical energy per unit distance in the z-direction for block (l) and $E(t)$ is the total energy for the entire system [58]. In (50)

the first term is the material kinetic energy and the second term is the elastic strain energy [58]. By rewriting the block energy (50) in terms of the mean stress $\bar{\sigma} = \sigma_{kk}/3$, the components of the deviatoric stress tensor $s_{ij} = \sigma_{ij} - \bar{\sigma}\delta_{ij}$, and the bulk modulus $K = \lambda + 2G/3$,

$$E^{(l)}(t) = \iint_{\widehat{\Omega}^{(l)}} \left[\frac{\rho}{2} v_i v_i + \frac{1}{4G} s_{ij} s_{ij} + \frac{1}{2K} \bar{\sigma}^2 \right] J d\xi_1 d\xi_2, \tag{51}$$

it is clear that $E^{(l)}(t) \geq 0$ if $\rho \geq 0$, $G \geq 0$, and $K \geq 0$.

Similarly, we introduce the semi-discrete energy by approximating the integrals in (50) with the $\boldsymbol{H}$ matrices from the SBP operators:

$$E_h(t) = \sum_l E_h^{(l)}(t), \tag{52}$$

$$E_h^{(l)}(t) = \frac{\rho}{2} \mathbf{v}_i^T \boldsymbol{J} \bar{\boldsymbol{H}} \mathbf{v}_i + \frac{1}{4G} \boldsymbol{\sigma}_{ij}^T \boldsymbol{J} \bar{\boldsymbol{H}} \left(\boldsymbol{\sigma}_{ij} - \frac{\lambda}{3\lambda + 2G} \boldsymbol{\sigma}_{kk} \delta_{ij} \right), \tag{53}$$

where $\bar{\boldsymbol{H}} = \boldsymbol{H}_1 \otimes \boldsymbol{H}_2$ can be interpreted as a quadrature rule for approximating the integrals in (50). Note that since we exclusively consider the diagonal norm SBP operators, i.e., $\boldsymbol{H}_i$ is diagonal, the matrices $\boldsymbol{J}$ and $\bar{\boldsymbol{H}}$ commute, and the product $\boldsymbol{J}\bar{\boldsymbol{H}}$ is symmetric.

With these definitions for the energy, we say that there is an energy estimate for the continuous and discrete problems if

$$E(t) \leq E(0), \qquad E_h(t) \leq E_h(0), \tag{54}$$

that is the energy at any future time is bounded by the initial energy in the solution; for more general definitions of well-posedness and energy estimates see Kreiss and Lorenz [32] and Gustafsson et al. [23]. In order to show that the energy estimate (54) holds for the continuous and discrete problems we will show that:

$$\frac{dE}{dt} \leq 0, \qquad \frac{dE_h}{dt} \leq 0, \tag{55}$$

and then (54) holds after integration.

Remark Due to the nonlinearity of the interface conditions, uniqueness of the solution does not follow directly from the energy estimate since the difference of two solutions does not satisfy the friction law [30]. The question of well-posedness for the most general problem of sliding between dissimilar elastic materials with rate-and-state friction laws is still an open and active research question [54]. Since the focus of this paper is the development of a stable numerical method, we do not consider this question further here.

4.1 Continuous Problem Energy Estimate

As noted above, an energy estimate for the continuous problem can be derived by looking at the energy dissipation rate for the problem. Namely, taking the time derivative of the continuous energy (49) gives

$$\frac{dE}{dt} = \sum_l \frac{dE^{(l)}}{dt}, \tag{56}$$

$$\frac{dE^{(l)}}{dt} = \iint_{\widetilde{\Omega}^{(l)}} \Bigg[\rho v_i \frac{\partial v_i}{\partial t} + \frac{1}{2G} \sigma_{ij} \frac{\partial \sigma_{ij}}{\partial t} - \frac{\lambda}{4G(3\lambda + 2G)} \delta_{ij} \left(\frac{\partial \sigma_{ij}}{\partial t} \sigma_{kk} + \sigma_{ij} \frac{d\sigma_{kk}}{dt} \right) \Bigg] J d\xi_1 d\xi_2. \tag{57}$$

Plugging in the governing equations (5) and (6) gives, after some straightforward algebra,

$$\begin{aligned} \frac{dE^{(l)}}{dt} &= \iint_{\widetilde{\Omega}^{(l)}} \left\{ \gamma \left[v_i \frac{\partial}{\partial \xi_\alpha} \left(J \frac{\partial \xi_\alpha}{\partial x_j} \sigma_{ij} \right) + \sigma_{ij} \frac{\partial}{\partial \xi_\alpha} \left(J \frac{\partial \xi_\alpha}{\partial x_j} v_i \right) \right] \right. \\ &\quad \left. + (1-\gamma) J \frac{\partial \xi_\alpha}{\partial x_j} \left(v_i \frac{\partial \sigma_{ij}}{\partial \xi_\alpha} + \sigma_{ij} \frac{\partial v_i}{\partial \xi_\alpha} \right) \right\} d\xi_1 d\xi_2 \\ &= \iint_{\widetilde{\Omega}^{(l)}} \left[\frac{\partial}{\partial \xi_\alpha} \left(J \frac{\partial \xi_\alpha}{\partial x_j} v_i \sigma_{ij} \right) - \frac{1}{2} (1-2\gamma) v_i \sigma_{ij} \frac{\partial}{\partial \xi_\alpha} \left(J \frac{\partial \xi_\alpha}{\partial x_j} \right) \right] d\xi_1 d\xi_2. \end{aligned} \tag{58}$$

Using the metric relations (4) it follows that

$$\frac{\partial}{\partial \xi_\alpha} \left(J \frac{\partial \xi_\alpha}{\partial x_j} \right) = 0, \tag{59}$$

and thus the last term cancels regardless of the choice of γ; this is as expected since all choices of γ yield the same continuous problem. Using this along with the divergence theorem the energy dissipation rate (58) becomes

$$\begin{aligned} \frac{dE^{(l)}}{dt} &= \int_0^1 \left[J \frac{\partial \xi_1}{\partial x_j} v_i \sigma_{ij} \right]_{\xi_1=0}^1 d\xi_2 + \int_0^1 \left[J \frac{\partial \xi_2}{\partial x_j} v_i \sigma_{ij} \right]_{\xi_2=0}^1 d\xi_1 \\ &= \int_{\partial \Omega^{(l)}} v_i \sigma_{ij} n_j ds, \end{aligned} \tag{60}$$

where we have transformed back to an integral over the block edge $\partial \Omega^{(l)}$ with ds being the arc length. The integrand can be rewritten as

$$v_i \sigma_{ij} n_j = v_i T_i = -v_n \sigma_n + v_m \tau_m + v_z \tau_z, \tag{61}$$

which is the rate of work per unit surface area done on the block edge by boundary tractions [38].

The block edge can be either an outer boundary or an interface (locked or frictional), and thus we derive the contribution from each of these conditions separately.

4.1.1 Outer Boundary

For outer boundaries the edge conditions take the form of $\mathbf{w}^+ = R\mathbf{w}^-$. Rewriting the physical variables in terms of the characteristic variables (30) and (31), the integrand becomes

$$\begin{aligned} -v_n \sigma_n + v_m \tau_m + v_z \tau_z &= \frac{1}{4Z_p} \left[\left(w_n^+ \right)^2 - \left(w_n^- \right)^2 \right] + \frac{1}{4Z_s} \left[\left(w_m^+ \right)^2 - \left(w_m^- \right)^2 \right] \\ &\quad + \frac{1}{4Z_s} \left[\left(w_z^+ \right)^2 - \left(w_z^- \right)^2 \right] \end{aligned}$$

$$= -\left(1 - R^2\right)\frac{1}{4}\left[\frac{(w_n^-)^2}{Z_p} + \frac{(w_m^-)^2}{Z_s} + \frac{(w_z^-)^2}{Z_s}\right]. \tag{62}$$

Since $-1 \leq R \leq 1$ this is negative semidefinite, and an energy estimate results if the edge is an outer boundary with the linear boundary condition.

4.1.2 Interface Conditions

If the edge is an interface, we consider two blocks (a) and (b) on either side of the interface. We thus consider the sum of the integrals from both blocks, which leads to the combined integrand

$$\begin{aligned} v_i^{(a)} T_i^{(a)} + v_i^{(b)} T_i^{(b)} &= \left(v_i^{(a)} - v_i^{(b)}\right) T_i^{(a)} \\ &= -\left(v_n^{(a)} + v_n^{(b)}\right)\sigma_n^{(a)} + \left(v_m^{(a)} + v_m^{(b)}\right)\tau_m^{(a)} \\ &\quad + \left(v_z^{(a)} - v_z^{(b)}\right)\tau_z^{(a)} \end{aligned} \tag{63}$$

where we have used the fact that the tractions across the interface are equal and opposite (36). In the case of the locked interface, the particle velocities are also continuous across the interface (37), and thus integrand (63) is zero.

All that is left to consider is the frictional interface condition. In this case, the normal component of velocity is continuous, and therefore (63) can be rewritten as

$$v_i^{(a)} T_i^{(a)} + v_i^{(b)} T_i^{(b)} = -\tau_m^{(a)} V_m - \tau_z^{(a)} V_z = -\boldsymbol{\tau}^T \mathbf{V}. \tag{64}$$

Applying the interface conditions (40) we have that

$$-\boldsymbol{\tau}^T \mathbf{V} = -\bar{\sigma}_n f(V, \psi) V \leq 0, \tag{65}$$

which is negative semidefinite since V, f, and $\bar{\sigma}_n$ are non-negative by definition. Thus we have an energy estimate for the continuous problem. Equation (65) represents the rate at which work is done on the fault.

4.2 Discrete Problem Energy Estimate

Here we use the energy method to pick penalty parameters for the semi-discretization such that the numerical method is stable. Furthermore, we will show that with our choice of penalty parameters the numerical scheme and continuous problem dissipate energy at rates that are identical up to the order of accuracy of the scheme. To do this, we will follow a completely analogous procedure as was used in the continuous energy estimate. Namely, we will take the time derivative of the discrete energy (53) and plug in the semi-discretization (19) and (20). We will then choose the penalty parameters T_p and T_s in the penalty terms (28) and (29) such that energy is dissipated at the correct rate, and thus stability follows.

Taking the time derivative of the discrete energy (53) and plugging in the semi-discretization (19) and (20) gives, after some algebra,

$$\begin{aligned} \frac{dE_h^{(l)}}{dt} &= \mathbf{v}_i^T \left[\gamma \bar{\boldsymbol{Q}}_\alpha \boldsymbol{J} \frac{\partial \xi_\alpha}{\partial x_j} + (1-\gamma)\boldsymbol{J}\frac{\partial \xi_\alpha}{\partial x_j}\bar{\boldsymbol{Q}}_\alpha\right]\boldsymbol{\sigma}_{ij} \\ &\quad + \boldsymbol{\sigma}_{ij}^T \left[\gamma \bar{\boldsymbol{Q}}_\alpha \boldsymbol{J} \frac{\partial \xi_\alpha}{\partial x_j} + (1-\gamma)\boldsymbol{J}\frac{\partial \xi_\alpha}{\partial x_j}\bar{\boldsymbol{Q}}_\alpha\right]\mathbf{v}_i \end{aligned}$$

$$+\rho \mathbf{v}_i^T \bar{\boldsymbol{H}}\big(\boldsymbol{\mathcal{P}}_i^N + \boldsymbol{\mathcal{P}}_i^s + \boldsymbol{\mathcal{P}}_i^E + \boldsymbol{\mathcal{P}}_i^W\big)$$
$$+\frac{1}{2G}\left(\boldsymbol{\sigma}_{ij}^T - \delta_{ij}\frac{\lambda}{3\lambda+2G}\boldsymbol{\sigma}_{kk}^T\right)\bar{\boldsymbol{H}}\big(\boldsymbol{\mathcal{P}}_{ij}^N + \boldsymbol{\mathcal{P}}_{ij}^s + \boldsymbol{\mathcal{P}}_{ij}^E + \boldsymbol{\mathcal{P}}_{ij}^W\big), \tag{66}$$

where for convenience we have made the following definitions

$$\bar{\boldsymbol{Q}}_1 = \boldsymbol{Q}_1 \otimes \boldsymbol{H}_2, \qquad \bar{\boldsymbol{Q}}_2 = \boldsymbol{H}_1 \otimes \boldsymbol{Q}_2. \tag{67}$$

In the continuous problem, the energy dissipation rate (58) was simplified using the metric relations and chain rule. This cannot be done for the discrete energy dissipation rate (66) as the discrete operators do not satisfy the chain rule. It is for this reason that we have introduced the splitting parameter γ. By making the choice $\gamma = 1/2$ the first two terms of (66), i.e., those that do not involve penalty parameters, become

$$\begin{aligned}
&\frac{1}{2}\mathbf{v}_i^T\left[\bar{\boldsymbol{Q}}_\alpha \boldsymbol{J}\frac{\partial \boldsymbol{\xi}_\alpha}{\partial x_j} + \boldsymbol{J}\frac{\partial \boldsymbol{\xi}_\alpha}{\partial x_j}\bar{\boldsymbol{Q}}_\alpha\right]\boldsymbol{\sigma}_{ij} + \frac{1}{2}\boldsymbol{\sigma}_{ij}^T\left[\bar{\boldsymbol{Q}}_\alpha \boldsymbol{J}\frac{\partial \boldsymbol{\xi}_\alpha}{\partial x_j} + \boldsymbol{J}\frac{\partial \boldsymbol{\xi}_\alpha}{\partial x_j}\bar{\boldsymbol{Q}}_\alpha\right]\mathbf{v}_i \\
&\quad = \frac{1}{2}\mathbf{v}_i^T\left[\big(\bar{\boldsymbol{Q}}_\alpha^T + \bar{\boldsymbol{Q}}_\alpha\big)\boldsymbol{J}\frac{\partial \boldsymbol{\xi}_\alpha}{\partial x_j} + \boldsymbol{J}\frac{\partial \boldsymbol{\xi}_\alpha}{\partial x_j}\big(\bar{\boldsymbol{Q}}_\alpha^T + \bar{\boldsymbol{Q}}_\alpha\big)\right]\boldsymbol{\sigma}_{ij} \\
&\quad = \mathbf{v}_i^T \boldsymbol{J}\frac{\partial \boldsymbol{\xi}_\alpha}{\partial x_j}\bar{\boldsymbol{B}}_\alpha \boldsymbol{\sigma}_{ij},
\end{aligned} \tag{68}$$

where we have defined

$$\bar{\boldsymbol{B}}_1 = \boldsymbol{B}_1 \otimes \boldsymbol{H}_2, \qquad \bar{\boldsymbol{B}}_2 = \boldsymbol{H}_1 \otimes \boldsymbol{B}_2, \tag{69}$$

with $\boldsymbol{B}_i = \boldsymbol{Q}_i + \boldsymbol{Q}_i^T$. The form of (68) exactly mimics the continuous energy estimate (60); of course nothing can be said about the sign of (68) since it does not include the penalty terms. Making a different choice for γ, such as the conventional choice of $\gamma = 1$, results in an energy growth term that will be of $\mathcal{O}(h^p)$ with sufficient refinement. This growth can destroy the accuracy of the solution for sufficiently long time integration (see Sect. 5 and Nordström and Carpenter [47]).

In order to determine the penalty terms, it is useful to perform a few intermediate calculations. Consider a single grid point (i, N_2) on the north edge, all other edges are handled in an analogous manner. Omitting the grid indices for clarity, in the energy dissipation rate (66) the penalty term involving velocity can be written as

$$\begin{aligned}
v_i \mathcal{P}_i^N &= -\frac{1}{T_p}v_n(v_n - \hat{v}_n) - \frac{1}{T_s}v_m(v_m - \hat{v}_m) - \frac{1}{T_s}v_z(v_z - \hat{v}_z) \\
&= -\frac{1}{T_p}\frac{(w_n^+ - w_n^-)}{2Z_p}\frac{(w_n^+ - \hat{w}_n^+)}{2Z_p} \\
&\quad -\frac{1}{T_s}\frac{(w_m^+ - w_m^-)}{2Z_s}\frac{(w_m^+ - \hat{w}_m^+)}{2Z_s} \\
&\quad -\frac{1}{T_s}\frac{(w_z^+ - w_z^-)}{2Z_s}\frac{(w_z^+ - \hat{w}_z^+)}{2Z_s},
\end{aligned} \tag{70}$$

where we have transformed from the physical variables to the characteristic variables using (30) and (31). In order to consider the penalty terms of (66) involving stress, we first note that

since the mean stress $\bar{\sigma}$ is an invariant of the stress tensor and $(\mathbf{n}, \mathbf{m}, \hat{\mathbf{z}})$ forms an orthonormal basis it follows that

$$3\bar{\sigma} = \sigma_{ii} = -\sigma_n + \sigma_m + \sigma_z. \tag{71}$$

We can then write

$$\sigma_{ij}\mathcal{P}_{ij}^N = \frac{1}{T_p}\left(\frac{3\lambda\bar{\sigma} - 2G\sigma_n}{\lambda + 2G}\right)(\sigma_n - \hat{\sigma}_n) - \frac{2}{T_s}\tau_m(\tau_m - \hat{\tau}_m) - \frac{2}{T_s}\tau_z(\tau_z - \hat{\tau}_z), \tag{72}$$

where we have used the fact that

$$\sigma_m - \hat{\sigma}_m = \sigma_z - \hat{\sigma}_z = -\left(1 - 2\frac{c_s^2}{c_p^2}\right)(\sigma_n - \hat{\sigma}_n) = -\frac{\lambda}{\lambda + 2G}(\sigma_n - \hat{\sigma}_n). \tag{73}$$

Additionally, we can write

$$\delta_{ij}\frac{\lambda}{3\lambda + 2G}\sigma_{kk}\mathcal{P}_{ij}^N = \frac{1}{T_p}\frac{3\lambda}{\lambda + 2G}\bar{\sigma}(\sigma_n - \hat{\sigma}_n). \tag{74}$$

Thus in (66) the penalty terms involving stress can be written as

$$\begin{aligned}
\frac{1}{2G}\left(\sigma_{ij} - \delta_{ij}\frac{\lambda}{3\lambda + 2G}\sigma_{kk}\right)\mathcal{P}_{ij}^N &= -\frac{1}{T_p(\lambda + 2G)}\sigma_n(\sigma_n - \hat{\sigma}_n) \\
&\quad - \frac{1}{T_s G}\tau_m(\tau_m - \hat{\tau}_m) - \frac{1}{T_s G}\tau_z(\tau_z - \hat{\tau}_z) \\
&= -\frac{1}{T_p(\lambda + 2G)}\frac{(w_n^+ + w_n^-)}{2}\frac{(w_n^+ + \hat{w}_n^+)}{2} \\
&\quad - \frac{1}{T_s G}\frac{(w_m^+ + w_m^-)}{2}\frac{(w_m^+ + \hat{w}_m^+)}{2} \\
&\quad - \frac{1}{T_s G}\frac{(w_z^+ + w_z^-)}{2}\frac{(w_z^+ + \hat{w}_z^+)}{2},
\end{aligned} \tag{75}$$

where once again we have used (30) and (31) to go from the physical variables to the characteristic variables. Similarly, (68) can be rewritten in characteristic form:

$$\begin{aligned}
\frac{\partial \xi_2}{\partial x_j}v_i\sigma_{ij} &= |\nabla\xi_2|(-v_n\sigma_n + v_m\sigma_m + v_z\sigma_z) \\
&= |\nabla\xi_2|\left\{\frac{1}{4Z_p}\left[\left(w_n^+\right)^2 - \left(w_n^-\right)^2\right] + \frac{1}{4Z_s}\left[\left(w_m^+\right)^2 - \left(w_m^-\right)^2\right]\right. \\
&\quad \left. + \frac{1}{4Z_s}\left[\left(w_z^+\right)^2 - \left(w_z^-\right)^2\right]\right\},
\end{aligned} \tag{76}$$

with no summation taken over repeated subscripts n, m, and z, and the gradient $\nabla\xi_2$ is taken with respect to the physical coordinate system x_i not the transformed coordinate system ξ_i.

Plugging (68), (70), (75), and (76) into the discrete energy estimate (66) gives

$$\left[\frac{dE_h^{(l)}}{dt}\right]_{(i,N_2)} = \frac{H_{11}J|\nabla\xi_2|}{4Z_p}\left[\left(w_n^+\right)^2 - \left(w_n^-\right)^2 - 2w_n^+\left(w_n^+ - \hat{w}_n^+\right)\right]$$

$$+\frac{H_{11}J|\nabla\xi_2|}{4Z_s}\left[\left(w_m^+\right)^2-\left(w_m^-\right)^2-2w_m^+\left(w_m^+-\hat{w}_m^+\right)\right]$$
$$+\frac{H_{11}J|\nabla\xi_2|}{4Z_s}\left[\left(w_z^+\right)^2-\left(w_z^-\right)^2-2w_z^+\left(w_z^+-\hat{w}_z^+\right)\right] \tag{77}$$

where we have chosen the penalty parameters (relaxation times) to be

$$T_p=\frac{H_{11}}{J|\nabla\xi_2|c_p},\qquad T_s=\frac{H_{11}}{J|\nabla\xi_2|c_s}, \tag{78}$$

where H_{11} is the first element of $\boldsymbol{H}_2$.

In order to show that (77) is negative semidefinite, note that

$$\left(w^+\right)^2-\left(w^-\right)^2-2w^+\left(w^+-\hat{w}^+\right)=\left(\hat{w}^+\right)^2-\left(w^-\right)^2-\left(w^+-\hat{w}^+\right)^2, \tag{79}$$

which holds for $w^\pm=w_n^\pm$, $w^\pm=w_m^\pm$, and $w^\pm=w_z^\pm$. The third term in (79) is a numerical dissipation term which is always negative semidefinite. Furthermore, this term will go to zero under refinement as w^+ approaches $\hat{w}^+$. Thus, in order to prove that the scheme is stable, we only need to show that $(\hat{w}^+)^2\le(w^-)^2$ so that (79) is negative semidefinite.

As in the continuous case, we consider the boundary and interface conditions separately.

4.2.1 Outer Boundary

If the edge is an outer boundary, then the edge conditions take the form of (34) with $\hat{w}^-=Rw^+$, and therefore

$$\left(\hat{w}^+\right)^2-\left(w^-\right)^2=-\left(1-R^2\right)\left(w^-\right)^2. \tag{80}$$

Since we constrain $-1\le R\le 1$ this is negative semidefinite. The total energy dissipation rate when grid node (i,N_2) is an outer boundary is then

$$\left[\frac{dE_h^{(l)}}{dt}\right]_{(i,N_2)}=-\left(1-R^2\right)\frac{H_{11}J|\nabla\xi_2|}{4}\left[\frac{(w_n^-)^2}{Z_p}+\frac{(w_m^-)^2}{Z_s}+\frac{(w_z^-)^2}{Z_s}\right]$$
$$-\frac{H_{11}J|\nabla\xi_2|}{4}\left[\frac{(w_n^+-\hat{w}_n^+)^2}{Z_p}+\frac{(w_m^+-\hat{w}_m^+)^2}{Z_s}+\frac{(w_z^+-\hat{w}_z^+)^2}{Z_s}\right], \tag{81}$$

which is negative semidefinite. Furthermore, the first term is of the same form as in the continuous problem (62) and the second term is the above mentioned numerical dissipation term. This numerical dissipation term will go to zero as the grid is refined and the grid data approaches the hat variables which strictly satisfy the boundary conditions. Thus, the numerical scheme and the continuous problem dissipate energy at the same rate up to the order of accuracy of the scheme.

4.2.2 Interface Conditions

In order to consider the case of an edge being an interface, we transform back to the physical variables:

$$\left(\hat{w}_n^+\right)^2-\left(w_n^-\right)^2=\left(\hat{w}_n^+-w_n^-\right)\left(\hat{w}_n^++w_n^-\right)=-4Z_p\hat{v}_n\hat{\sigma}_n, \tag{82}$$

$$\left(\hat{w}_m^+\right)^2 - \left(w_m^-\right)^2 = \left(\hat{w}_m^+ - w_m^-\right)\left(\hat{w}_m^+ + w_m^-\right) = 4Z_s\hat{v}_m\hat{\tau}_m, \tag{83}$$

$$\left(\hat{w}_z^+\right)^2 - \left(w_z^-\right)^2 = \left(\hat{w}_z^+ - w_z^-\right)\left(\hat{w}_z^+ + w_z^-\right) = 4Z_s\hat{v}_z\hat{\tau}_z. \tag{84}$$

Using these, the energy dissipation rate (66) becomes:

$$\left[\frac{dE_h^{(l)}}{dt}\right]_{(i,N_2)} = H_{11}J|\nabla\xi_2|\hat{T}_i\hat{v}_i - \frac{H_1 J|\nabla\xi_2|}{4}\left[\frac{(w_n^+ - \hat{w}_n^+)^2}{Z_p} + \frac{(w_m^+ - \hat{w}_m^+)^2}{Z_s} + \frac{(w_z^+ - \hat{w}_z^+)^2}{Z_s}\right]. \tag{85}$$

Considering only the first term and summing over both sides of the interface gives

$$H_{11}^{(a)}J^{(a)}\left|\nabla\xi_2^{(a)}\right|\hat{T}_i^{(a)}\hat{v}_i^{(a)} + H_{11}^{(b)}J^{(b)}\left|\nabla\xi_2^{(b)}\right|\hat{T}_i^{(b)}\hat{v}_i^{(b)} = H_{11}^{(a)}J^{(a)}\left|\nabla\xi_2^{(a)}\right|\left[-\left(\hat{v}_n^{(a)} + \hat{v}_n^{(b)}\right)\hat{\sigma}_n^{(a)} + \left(\hat{v}_m^{(a)} + \hat{v}_m^{(b)}\right)\hat{\tau}_m^{(a)} + \left(\hat{v}_z^{(a)} - \hat{v}_z^{(b)}\right)\hat{\tau}_z^{(a)}\right], \tag{86}$$

where we have used the fact that the tractions across the interface (for the hat variables) are equal and opposite (45). In the case of the locked interface, the hat variable particle velocities are also continuous across the interface (46), and thus (86) is zero.

In the case of frictional interfaces, only the normal component of velocity is continuous (see (48)), and therefore

$$J^{(a)}\left|\nabla\xi_2^{(a)}\right|\left(\hat{T}_i^{(a)}\hat{v}_i^{(a)} + \hat{T}_i^{(b)}\hat{v}_i^{(b)}\right) = -\hat{\tau}_m^{(a)}\hat{V}_m - \hat{\tau}_z^{(a)}\hat{V}_z = -\hat{\mathbf{V}}^T\hat{\boldsymbol{\tau}}^{(a)}. \tag{87}$$

Though in general the grid data will not satisfy the friction law, the hat variables $\hat{\mathbf{V}}$ and $\hat{\boldsymbol{\tau}}^{(a)}$ have been constructed such that they exactly satisfy the friction law (see (47)):

$$-\hat{\mathbf{V}}^T\hat{\boldsymbol{\tau}}^{(a)} = -\hat{\bar{\sigma}}_n f(\hat{V}, \psi)\hat{V} \le 0. \tag{88}$$

Since this is negative semidefinite, we have an energy estimate and stability follows. Equation (88) is of the same form as the energy dissipation in the continuous problem (65), and thus, even in the case of nonlinear interface conditions, the discrete and continuous solutions dissipate energy at the same rate up to the order of accuracy of the scheme.

5 Computational Results

To confirm the above stability and accuracy results we test the method (and the code which implements the method) in two ways. In order to rigorously verify the accuracy, convergence, and stability properties of the method the method of manufactured solutions (MMS) [55] is used. In MMS, boundary data (forcing functions) and source terms are added to the problem in such a way that the exact solution is known a priori. In the second test we apply the method to an extremely challenging application problem—a subduction zone megathrust earthquake—involving a highly irregular domain, complex free surface topography, multiple blocks with different material properties, and a nonplanar fault.

In all the results that follow, the mesh is generated using the transfinite interpolation method [27] after specifying the location of the points (and outward pointing normals) on the boundaries and faults. The metric derivatives (e.g., $\partial x_i/\partial\xi_\alpha$) are computed using the same SBP difference operators used in the semi-discrete approximation.

As formulated, the method can encompass all two-dimensional problems, including both plane strain (mode II ruptures), antiplane shear (mode III ruptures), and even mixed mode

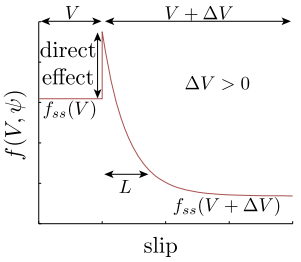

Fig. 2 Response of the friction coefficient, f, to an abrupt increase in slip velocity from V to $V + \Delta V$, for a friction law that is instantaneously velocity-strengthening ($\partial f(V, \psi)/\partial V > 0$) with a velocity-weakening steady state ($df_{ss}(V)/dV < 0$). f instantaneously increases from the steady state value $f_{ss}(V)$ (the direct effect), then evolves with slip over the state evolution distance, L, to the new, lower steady state value $f_{ss}(V + \Delta V)$

shear ruptures. However, both tests are restricted to plane strain deformation in the x_1- and x_2-directions only, for which only P and SV waves are excited. Convergence tests for the antiplane shear problem were conducted by Kozdon et al. [30].

5.1 Rate-and-State Friction and Nondimensionalization

Before proceeding to the computational results, we first present the specific rate-and-state friction law used in this work and cast the problems in nondimensional form.

We use the regularized slip law form of rate-and-state friction [35, 52]:

$$f(V, \psi) = a \operatorname{arcsinh}\left(\frac{V}{2V_0} \exp\left(\frac{\psi}{a}\right)\right), \qquad \frac{d\psi}{dt} = -\frac{V}{L}\big[f(V, \psi) - f_{ss}(V)\big], \tag{89}$$

where L is the state evolution distance, V_0 is an arbitrary reference velocity, and a is the direct effect parameter. Experiments and theory demonstrate that $a > 0$ [54], corresponding to an instantaneous strengthening of the fault following an abrupt increase in V, as illustrated in Fig. 2. Following the direct effect, $f(V, \psi)$ evolves toward $f_{ss}(V)$ over a characteristic slip distance L. For the steady state friction coefficient, we use the standard logarithmic form

$$f_{ss}(V) = f_0 - (b - a) \ln\left(\frac{V}{V_0}\right), \tag{90}$$

where f_0 is the steady state friction coefficient at $V = V_0$ and the sign of $b - a$ determines whether the fault is velocity-strengthening ($b - a < 0$) or velocity-weakening ($b - a > 0$) in steady state. The latter is necessary for unstable slip and self-sustaining rupture propagation.

We next nondimensionalize the equations using the assumption that at least some portion of the fault is velocity-weakening in steady state (so $b - a > 0$). The state evolution distance, L, provides a characteristic slip distance. A linear stability analysis of steady sliding along a planar frictional interface with $b - a > 0$ between identical elastic half-spaces [53, 54] reveals that pertubations having along-fault wavelengths exceeding a critical wavelength are unstable; shorter wavelength perturbations are stable. (And if $b - a < 0$ then the interface is stable to all perturbations as long as $a \geq 0$.) For quasi-static elasticity, the critical wavelength is approximately $h^* = GL/(b - a)\sigma_n^0$, and we take this as the characteristic distance scale. The associated time scale is $T = h^*/c_s$. The grid spacing (along the fault) must be smaller

than h^* so that the unresolved (Nyquist) modes in the solutions cannot trigger this physical instability.

For propagating ruptures, inertial terms become important in the momentum balance and h^* no longer provides an accurate characterization of spatial variations in the solution. In particular, fields vary most rapidly in the region immediately behind the propagating rupture front, where the strength drop occurs. The strength drop occurs over a distance, R, that is proportional to h^*, but about three orders of magnitude smaller than h^* for typical parameters. For more discussion of R and h^*, see Rice et al. [54] and Dunham et al. [17].

We therefore nondimensionalize space and time as

$$\bar{x_i} = \frac{x_i}{h^*}, \qquad \bar{t} = \frac{t}{T}. \tag{91}$$

The nondimensional grid spacing must satisfy $\bar{h} \ll 1$ (in the vicinity of the fault). Stresses and particle velocities are related via the shear impedance, Z_s, leading to the nondimensionalization

$$\bar{\sigma}_{ij} = \frac{\sigma_{ij}}{(b-a)\sigma_n^0}, \qquad \bar{v}_i = \frac{Z_s v_i}{(b-a)\sigma_n^0}, \quad \text{and} \quad \bar{V} = \frac{Z_s V}{2(b-a)\sigma_n^0}. \tag{92}$$

In the case of dissimilar materials, a choice must be made for Z_s from one side of the interface in the nondimensionalization.

For the friction law, we select the reference slip velocity as $V_0 = 2(b-a)\sigma_n^0/Z_s$, which leads to the dimensionless form

$$f = a \operatorname{arcsinh}\left(\frac{\bar{V}}{2}\exp\left(\frac{\psi}{a}\right)\right), \tag{93}$$

$$\frac{d\psi}{d\bar{t}} = -\bar{V}\big[f(\bar{V},\psi) - f_{ss}(\bar{V})\big], \quad f_{ss}(\bar{V}) = f_0 - (b-a)\ln(\bar{V}). \tag{94}$$

Thus in the friction law we have three nondimensional parameters: a, $b-a$, and f_0. The equations also require an initial value for ψ.

As noted in Sect. 3.4, the state variable ψ is integrated using the hat variables (24). This is done so that state and the interface relations are integrated in a consistent manner. Additionally, this avoids any complications with the fact that the traction components of stress, as defined by the grid values, will not be continuous across the interface when the SAT method is used.

5.2 Method of Manufactured Solutions

We consider a two block system with a frictional fault interface. The geometry of the two blocks is shown in Fig. 3. As can be seen, the blocks are transformed in all directions and across the fault interface the coordinate transform is continuous but not smooth. We next construct an MMS solution that satisfies continuity of traction components of stress across the fault ($\bar{T}_i^{(a)} = -\bar{T}_i^{(b)}$), the non-opening condition ($\bar{v}_n^{(a)} + \bar{v}_n^{(b)} = 0$), and parallel slip velocity and shear stress. (Of course, this is not strictly necessary, but facilitates verification of our implementation.) Since we only consider in-plane deformation, $\bar{\tau}_z = \bar{V}_z = 0$, and the parallel requirement reduces to $\operatorname{sign}(\bar{V}_m) = \operatorname{sign}(\bar{\tau}_m)$.

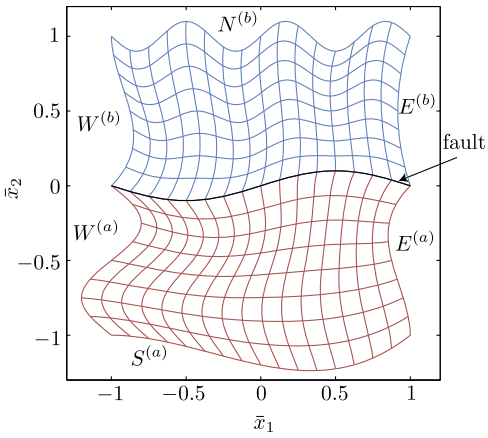

Fig. 3 Computational domain for the MMS calculation. The expression for the block edges are given in terms of the transformed variables ξ_1 and ξ_2 with the transfinite interpolation method [27] used to define the interior transform

side	$\bar{x}_1(\xi_1,\xi_2)$	$\bar{x}_2(\xi_1,\xi_2)$
fault	$2\xi_1-1$	$-\sin(2\pi\xi_1)/10$
$S^{(a)}$	$2\xi_1-1$	$4\xi_1^2(2\xi_1-2)/5-1$
$W^{(a)}$	$-\sin(2\pi\xi_2)/5-1$	ξ_2-1
$E^{(a)}$	$(\xi_2-1)\xi_2^2+1$	ξ_2-1
$N^{(b)}$	$2\xi_1-1$	$-\sin(6\pi\xi_1)/10+1$
$W^{(b)}$	$\xi_2(\xi_2-1)^2-1$	ξ_2
$E^{(b)}$	$\xi_2(\xi_2-1)/3+1$	ξ_2

The fault is given by the curve $\bar{x}_1 = 2\xi_1 - 1$ and $\bar{x}_2 = \kappa(\xi_1)$ with $\kappa(\xi_1) = -\sin(2\pi\xi_1)/10$. The unit normal and perpendicular vectors to the fault are then

$$\mathbf{n}^{(b)} = -\mathbf{n}^{(a)} = \frac{1}{\sqrt{4+\kappa'(\xi_1)^2}}\begin{bmatrix}\kappa'(\xi_1)\\ -2\end{bmatrix}, \tag{95}$$

$$\mathbf{m}^{(b)} = -\mathbf{m}^{(a)} = \frac{-1}{\sqrt{4+\kappa'(\xi_1)^2}}\begin{bmatrix}2\\ \kappa'(\xi_1)\end{bmatrix}. \tag{96}$$

To define the solution we introduce the following auxiliary functions:

$$\varsigma_{nn}(\bar{x}_1,\bar{x}_2,\bar{t}),\ \varsigma_m^{(l)}(\bar{x}_1,\bar{x}_2,\bar{t}),\ \varsigma_{nm}(\bar{x}_1,\bar{x}_2,\bar{t}),\ \varphi_n(\bar{x}_1,\bar{x}_2,\bar{t}),\ \varphi_m^{(l)}(\bar{x}_1,\bar{x}_2,\bar{t}), \tag{97}$$

which are all continuous functions of space and time, except for discontinuities in $\varsigma_m^{(l)}$ and $\varphi_m^{(l)}$ across the fault. The solution in the entire domain is

$$\bar{\sigma}_{xx}^{(l)} = -\varsigma_{nn}m_2^2 + \varsigma_m^{(l)}n_2^2 - 2\varsigma_{nm}m_2n_2, \tag{98}$$

$$\bar{\sigma}_{yy}^{(l)} = -\varsigma_{nn}m_1^2 + \varsigma_m^{(l)}n_1^2 - 2\varsigma_{nm}m_1n_1, \tag{99}$$

$$\bar{\sigma}_{xy}^{(l)} = \varsigma_{nn}m_1m_2 - \varsigma_m^{(l)}n_1n_2 + \varsigma_{nm}(n_2m_1 + n_1m_2), \tag{100}$$

$$\bar{v}_1^{(l)} = \varphi_m^{(l)}n_2 - \varphi_n m_2, \qquad \bar{v}_2^{(l)} = -\varphi_m^{(l)}n_1 + \varphi_n m_1, \tag{101}$$

$$m_1 = -n_2 = m_1^{(a)}, \qquad m_2 = n_1 = m_2^{(b)}. \tag{102}$$

It is easy to verify that this solution yields fault values: $\bar{v}_n^{(a)} + \bar{v}_n^{(b)} = 0$, $\bar{\tau} = \varsigma_{nm}$, $\bar{\sigma}_n = -\varsigma_{nn}$, and $\bar{V} = \varphi_m^{(a)} - \varphi_m^{(b)}$.

In order to test both the implementation of the finite difference method as well as state evolution we use a slightly modified frictional framework. Namely, we use the friction law:

$$f = a \operatorname{arcsinh}\left(\frac{\bar{V}}{2}\exp\left(\frac{\psi^* + \delta\psi}{a}\right)\right), \tag{103}$$

$$\frac{d\delta\psi}{d\bar{t}} = -\bar{V}\left[f\left(\bar{V}, \psi^* + \delta\psi\right) - f_{ss}(\bar{V})\right] + \bar{V}^*\left[f\left(\bar{V}^*, \psi^*\right) - f_{ss}\left(\bar{V}^*\right)\right], \tag{104}$$

$$\psi^* = \ln\left(\frac{2}{\bar{V}^*}\sinh\left(\frac{\bar{\tau}^*}{a\bar{\sigma}_n^*}\right)\right), \tag{105}$$

where the superscript $*$ indicates fields that are known functions of space and time evaluated using the exact solution (98)–(101). For the outer boundary conditions we specify the incoming characteristic variables, namely $\mathbf{w}^{+(l)} = \mathbf{g}$ on $\partial\Omega$ where $\mathbf{g}$ is easily defined from (98)–(101) using the outward pointing normal.

For our test we define the auxiliary functions to be

$$\varsigma_{nn} = -\varsigma_{nn}^g g(\bar{x}_1, \bar{x}_2, \bar{t}) - \varsigma_{nn}^0, \qquad \varsigma_{nm} = \varsigma_{nm}^g g(\bar{x}_1, \bar{x}_2, \bar{t}), \tag{106}$$

$$\varsigma_m^{(a)} = -\varsigma_m^g g(\bar{x}_1, \bar{x}_2, \bar{t}), \qquad \varsigma_m^{(b)} = \varsigma_m^g g(\bar{x}_1, \bar{x}_2, \bar{t}), \tag{107}$$

$$\varphi_m^{(a)} = -\varphi_m^g g(\bar{x}_1, \bar{x}_2, \bar{t}), \qquad \varphi_m^{(b)} = \varphi_m^g g(\bar{x}_1, \bar{x}_2, \bar{t}), \tag{108}$$

$$\varphi_n = \varphi_n^g g(\bar{x}_1, \bar{x}_2, \bar{t}), \qquad g(\bar{x}_1, \bar{x}_2, \bar{t}) = \cos(\bar{k}\bar{x}_1)\cos(\bar{k}\bar{x}_2)\cos(\bar{\omega}\bar{t}), \tag{109}$$

with $\bar{k} = 2\pi$, $\bar{\omega} = 200\pi/69$, $\varsigma_{nn}^0 = 250$, $\varsigma_{nn}^g = 125$, $\varsigma_{nm}^g = \varsigma_m^g = 150$, and $\varphi_m^g = \varphi_m^g = 5$. The domain given in Fig. 3 is discretized using $N_1 = 2N_2 = 2^i$ where $i = 7, 8, 9, 10$. The simulation is run until $\bar{t}_f = 13.8$ which corresponds to $\bar{t}_f\bar{\omega}/2\pi = 20$ oscillations of the solution. The material is identical on both sides of the fault with a Poisson ratio of $\nu = 0.21875$. Time integration is performed with a 4th order, low memory Runge-Kutta method of Carpenter and Kennedy [9] (their 5[4] method with solution 3) using a time step size $\Delta\bar{t} = 0.4416/N_1 \approx 0.3\bar{h}_{\min}$, where

$$\bar{h}_{\min} = \min_{\xi_1,\xi_2}\left[\min\left(\frac{J}{N_1}\sqrt{\left(\frac{\partial x_1}{\partial \xi_2}\right)^2 + \left(\frac{\partial x_2}{\partial \xi_1}\right)^2}, \frac{J}{N_2}\sqrt{\left(\frac{\partial x_1}{\partial \xi_1}\right)^2 + \left(\frac{\partial x_2}{\partial \xi_2}\right)^2}\right)\right]. \tag{110}$$

The error in the solution is defined as

$$\text{error}(N_1) = \|\mathbf{q} - \mathbf{q}^*\|_h, \tag{111}$$

where the norm $\|\cdot\|_h$ is the energy norm defined in (52) and $\mathbf{q}^*$ is the exact solution evaluated at the same spatial locations as the discrete solution. We estimate the convergence rate between successive solutions as

$$\text{p}(N_1) = \log_2\left(\frac{\text{error}(N_1/2)}{\text{error}(N_1)}\right). \tag{112}$$

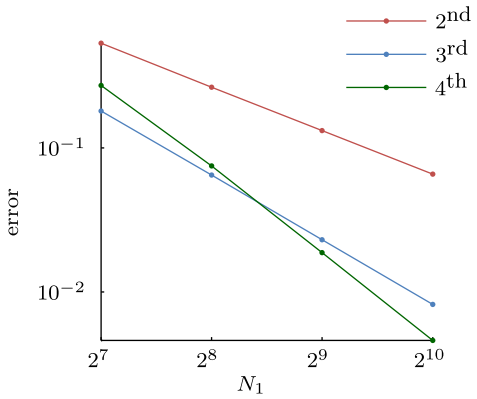

	2nd		3rd		4th	
N_1	error	rate	error	rate	error	rate
2^6	2.84×10^{0}	···	3.24×10^{0}	···	7.36×10^{0}	···
2^7	6.96×10^{0}	2.03	4.19×10^{-1}	2.96	5.63×10^{-1}	3.71
2^8	1.73×10^{0}	2.01	5.32×10^{-2}	2.98	3.51×10^{-2}	4.00
2^9	4.32×10^{-1}	2.00	6.69×10^{-3}	2.99	2.13×10^{-3}	4.04

Fig. 4 Global error in the H-norm and convergence rate estimates for the method of manufactured solutions (Color figure online)

Fig. 5 Error for the conservative ($\gamma = 1$) method and the energy stable ($\gamma = 1/2$) method versus time (Color figure online)

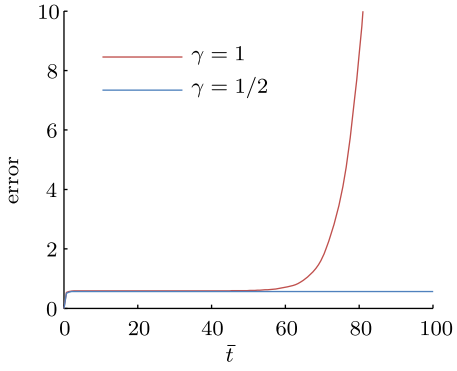

The results for the 2nd, 3rd, and 4th order diagonal SBP operators [33, 34, 59] are given in Fig. 4, which shows the error as a function of N_1 and the estimated convergence rates.

In order to assess the importance of energy stability, particularly for long time integration, Fig. 5 compares the energy stable ($\gamma = 1/2$) method with the non-energy stable, fully conservative ($\gamma = 1$) method; see Sect. 4.2. Shown in the figure is the error in the solution for the $N_1 = 2^7$ simulation versus time for both schemes using the globally 4th order accurate SBP operator. As can be seen, the error grows rapidly in time after sufficiently long time. The effects of this energy growth are not seen at earlier times, since the growth is related to a lack of a discrete chain rule and thus the growth rate should be of order $\mathcal{O}(h^4)$ [47].

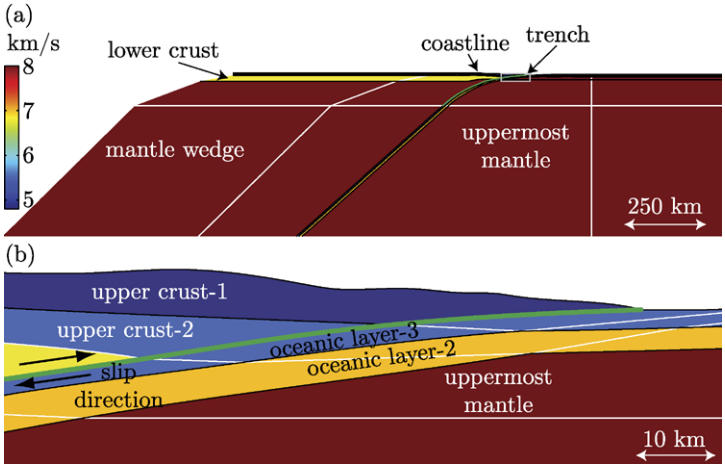

Layer Name	P-wave velocity (km/s)	S-wave velocity (km/s)	Density (kg/m^3)	Shear modulus (GPa)
upper crust-1	4.8	2.8	2200	16.9
upper crust-2	5.5	3.2	2600	26.2
lower crust	7.0	4.0	2800	45.7
mantle wedge	8.0	4.6	3200	68.3
oceanic layer-3	5.5	3.2	2600	26.2
oceanic layer-2	6.8	3.9	2800	43.1
uppermost mantle	8.0	4.6	3200	68.3

Fig. 6 (**a**) Subduction zone geometry for megathrust earthquake problem. The *color scale* denotes the P-wave velocity structure. *Solid black lines* denote different material boundaries whereas white lines denote computational (multi-block grid) boundaries. The fault is denoted by a *thick green line*. (**b**) Close view of the geometry near the trench axis. The accompanying table lists material properties (Color figure online)

5.3 Subduction Zone Megathrust Earthquake

We now consider a complex application problem to demonstrate the full potential of the method. The problem is motivated by the 11 March 2011 magnitude 9.0 Tohoku, Japan, megathrust earthquake and the resulting tsunami. The specific geometry we consider is shown in Fig. 8, and is based on the subduction zone structure in the vicinity of the Japan trench [40, 41]. The Pacific Plate is being subducted to the west beneath the North American/Okhotsk Plate, with relative motion across the plate interface (the fault) occurring during megathrust earthquakes. The Japanese island of Honshu lies at the left edge of the domain, and the upper boundary of the entire computational domain is the seafloor (with the ocean deepening offshore until it reaches a maximum depth of about 7 km at the trench). Slip along the plate interface causes vertical deformation of the seafloor, causing uplift or subsidence of the overlying water layer. Gravity waves (tsunamis) occur as the sea surface returns to an equilibrium level. The model used for this example is similar to the geometry used in Kozdon and Dunham [29] except a slightly different frictional description is used.

The east (Pacific Plate) side is idealized with a three-layer model (two oceanic layers and the uppermost mantle). As the Pacific Plate dives beneath the North American/Okhotsk Plate, it crosses several material layers (idealized here as upper and lower crust and the

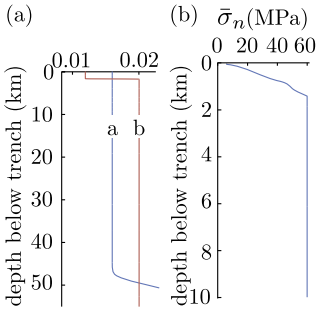

parameter		value
steady state friction at V_0	f_0	0.3
reference velocity	V_0	10^{-6} m/s
initial state variable	ψ_0	0.5
state evolution distance	L	0.4 m

Fig. 7 (**a**) Frictional parameters and (**b**) the effective normal stress for the subduction megathrust problem

mantle wedge). We do not include an ocean water layer in this model (it makes negligible difference in the rupture process due to the large impedance contrast between water and rock [28]), and instead approximate the seafloor as a traction-free surface.

Figure 6 shows the multi-block structure used for this example, with black lines representing interfaces across which there is a material contrast and white lines representing purely computational interfaces. In this model there are 30 blocks and 49 interfaces, four of which are frictional interfaces.

Initial conditions are required on stress, velocity, and state variable. We take the initial velocity to be everywhere zero. We write the stress as the superposition of a prestress, σ_{ij}^0, and stress perturbations arising from slip on the fault, $\Delta\sigma_{ij}$. Linearity of the elastic wave equation permits us to solve only for stress perturbations in the interior, but the nonlinear friction law must be enforced using the absolute stress values. Hence we write the shear and normal stresses used in the friction law (40) as $\tau = \tau_0 + \Delta\tau$ and $\sigma_n = \sigma_0 + \Delta\sigma_n$, respectively, where the prestress values τ_0 and σ_0 are known functions and the stress changes are calculated from wave propagation in the interior. This procedure is similar to adding forcing functions on the interface as done in the MMS test problem.

We take the background normal stress to be linearly increasing with depth to a maximum value of $\sigma_0 = 60$ MPa (see Fig. 7). We take the initial shear stress to be $\tau_0 = 0.3\sigma_0$ (except in the nucleation zone, as described below). Similarly, the friction parameters vary with temperature and rock type (and thus with depth), and in this model we use the profile given in Fig. 7. With these values of a and $b-a$, the rupture will propagate up the fault toward the free surface, but since $b-a$ becomes negative at depth, the downward rupture will eventually stop as the fault becomes velocity-strengthening. The fault is also velocity strengthening near the trench.

In order to nucleate, or start, the rupture, the initial shear stress is increased over a small patch of the fault:

$$\tau_0 = 0.3\sigma_0 + 42\ \text{MPa} \exp\left[-\frac{(x_1 + 155\ \text{km})^2 + (x_2 - 30\ \text{km})^2}{2(1.75\ \text{km})^2}\right]. \tag{113}$$

The stress perturbation immediately initiates rapid sliding via the direct effect (shear stress and slip velocity increase together), since state evolution is negligible over short time scales. Because the amplitude and width of the Gaussian perturbation are sufficiently large, the perturbation grows and leads to unstable slip and dynamic rupture.

To assess solution accuracy, we conduct the simulation at two levels of resolution. The low resolution run has $\sim 8.9 \times 10^6$ grid points (4403 in the ξ_1-direction and 2015 in the ξ_2-direction) with a minimum grid spacing along the fault of 200 m. We minimize the effects

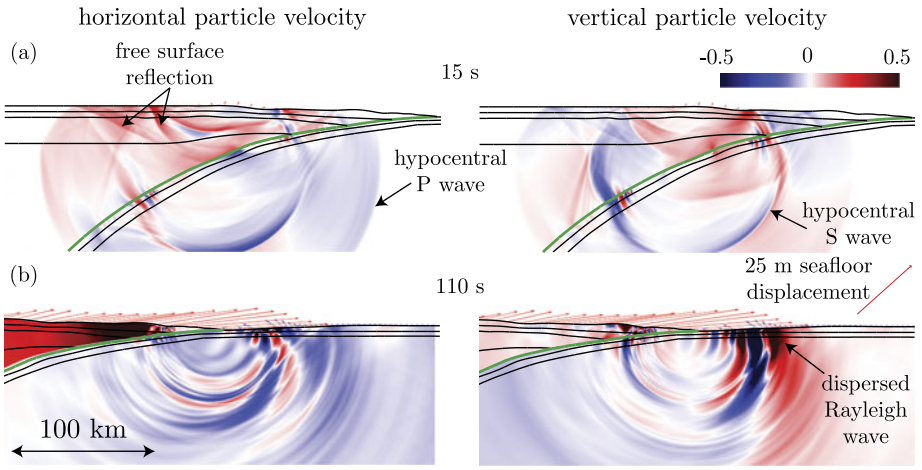

Fig. 8 (**a**) Wavefield at $t = 15$ s for the subduction zone megathrust earthquake. The actively slipping part of the fault lies slightly behind the hypocentral S-wave front. (**b**) Wavefield at $t = 110$ s shortly after the rupture has reached the trench. (**a**) and (**b**) have the same color and length scale. The *arrows* on the free surface show the seafloor deformation (*red* and *blue arrows* are for points west and east of the trench, respectively)

of the outer boundaries by using a linear grid stretching for those blocks which border the absorbing boundary. This grid structure results in minimum and maximum grid spacings $h_{\min} = 4$ m and $h_{\max} = 9.7$ km, respectively, where $h_{\min}$ is defined in (110) and $h_{\max}$ is defined similarly. The time step is $\Delta t = 2.5 \times 10^{-4}$ s, corresponding to an S-wave CFL of 0.3. The 200 s simulation requires 8×10^5 time steps. The high resolution run has twice the grid resolution ($\sim 3.5 \times 10^7$ grid points and 1.6×10^6 time steps).

Figure 8(a) shows the wavefield at 15 s. The relative motion of the North American/Okhotsk Plate and the Pacific Plate is consistent with the sense of slip indicated in Fig. 6. For the Japan trench, the island arc would be on the North American/Okhotsk Plate side, approximately 250 km from the trench axis (the intersection of the fault with the seafloor). Figure 8(b) shows the wavefield at 95 s, shortly after the rupture has reached the trench. The material on the North American/Okhotsk Plate side is moving rapidly to the right due to interaction of the waves reflected off the seafloor with the subducting plate interface. The wavefield is quite rich in structure, and includes dispersed Rayleigh waves propagating along the seafloor in the oceanic layers. These details are lost in models that simplify the physics and geometric complexity.

An important seismological quantity is the cumulative slip on the fault, which partially determines the magnitude of the earthquake. Slip is often estimated in inversion studies using geodetic and seismic data. We show the cumulative slip, plotted every 5 s, in Fig. 9 for the two resolution levels. At the end of the simulations (200 s) the maximum difference in slip between the two simulations is 0.4 % relative to the mean slip and 0.2 % on average. During the simulation the largest difference in slip is around the rupture tip.

In Fig. 10 the final vertical and horizontal displacement of the ocean floor is shown (arrows on free surface in Fig. 8 show the cumulative displacement at the wavefield snapshot times). The seafloor displacement is critical for tsunami prediction and hazard assessment, as this is what causes the initial perturbation to the water column. Our model results match the structure and magnitude of uplift seen in the observed data from the Tohoku earthquake [29, 57].

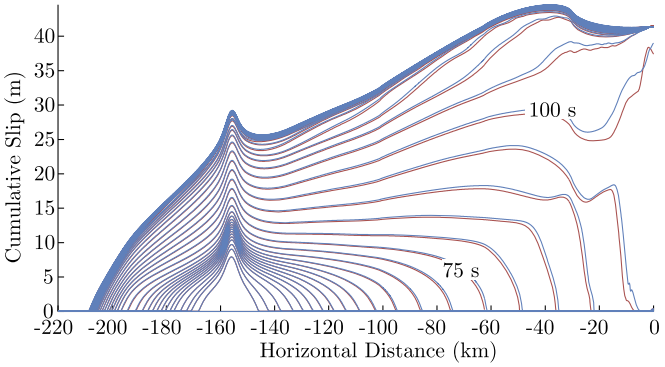

Fig. 9 Cumulative slip as a function of distance along the fault, plotted at 5 s intervals. The *solid red line* is the base resolution simulation and the *blue line* is a simulation at twice the resolution. The earthquake is nucleated at approximately −155 km along the fault and the trench/free surface is at 0 km (Color figure online)

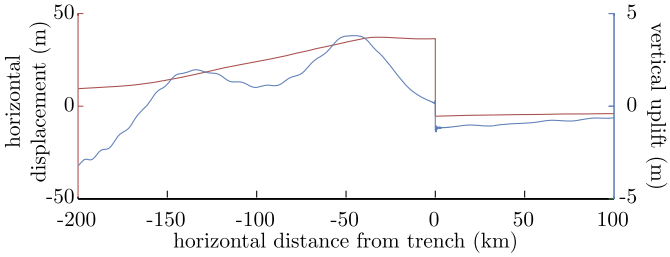

Fig. 10 Vertical (*blue line*) and horizontal (*red line*) seafloor displacement at $t = 200$ s as a function of horizontal distance (see Fig. 8). The fault reaches the seafloor at 0 km (Color figure online)

6 Conclusions

We have developed a numerical method for simulation of earthquake ruptures in complex geometries. The method uses coordinate transforms and multi-block meshes to handle irregular domains. Additionally, this allows the accurate coupling of material blocks across discontinuous changes in material properties. Though not shown, as it was outside the focus of the paper, this includes the coupling of elastic and acoustic blocks. The method is based on the SBP-SAT formalism, and is provably stable with appropriately chosen penalty parameters.

Furthermore, we have developed a splitting for coordinate transforms which ensures energy stability for arbitrary coordinate transforms. This eliminates the additional energy growth in the numerical solution seen in previous work with coordinate transforms [46, 47]. Though worked out for the equations of linear elasticity, the splitting is straightforward to apply to any linear hyperbolic system.

The accuracy and stability of the numerical method were verified using the method of manufactured solutions for a plane strain problem; the accuracy of the method for antiplane shear deformation was previously demonstrated by Kozdon et al. [30]. Additionally, it was shown that the energy growth due to using the standard, conservative formulation destroys the accuracy of the solution on the highly skewed meshes used for this problem, thus demon-

strating the need for an energy stable method as developed in this paper. A realistic application problem involving a subduction zone megathrust earthquake through multiple material layers demonstrated the versatility of the method for extremely challenging geometries.

The method developed in this paper has been successfully used in several simulation studies of the physics governing earthquake dynamics. Kozdon and Dunham [29] simulated the 11 March 2011 Tohoku, Japan, megathrust earthquake with realistic material properties and geometry using the method described in this paper. This allowed Kozdon and Dunham [29] to make direct comparisons with seafloor deformation data and slip inversions as well as demonstrate that rupture to the seafloor is possible for subduction zone megathrust earthquakes even when the near trench fault segment is velocity strengthening. Similarly, the method was used in Dunham et al. [18] to explore the role of fault roughness on earthquake dynamics.

Acknowledgements J.E.K. and E.M.D. were supported by National Science Foundation (NSF) award EAR-0910574 and the Southern California Earthquake Center (SCEC), as funded by NSF Cooperative Agreement EAR-0529922 and US Geological Survey Cooperative Agreement 07HQAG0008 (SCEC contribution number 1424). J.E.K. was also supported by NSF Fellowship for Transformative Computational Science using CyberInfrastructure OCI-1122734. The computations in this paper were conducted at the Stanford Center for Computational Earth and Environmental Science. Finally, we would like to thank the two anonymous reviewers of the manuscript for their suggestions and comments.

Appendix: Equivalence of Friction Law in Physical and Characteristic Variables

In this appendix we show that if $\partial f/\partial V \geq 0$ then friction law $f(V,\psi)$ is expressible in characteristic form. Assuming that the interface is between blocks (a) and (b), the normal stress and fault normal velocity can be written using the characteristic interface variables (30):

$$\sigma_n^{(a)} = -\frac{1}{2}\big(w_n^{+(a)} + \mathcal{W}_n^{-(a)}\big), \qquad \sigma_n^{(b)} = -\frac{1}{2}\big(w_n^{+(b)} + \mathcal{W}_n^{-(b)}\big), \tag{114}$$

$$v_n^{(a)} = \frac{1}{2Z_p^{(a)}}\big(w_n^{+(a)} - \mathcal{W}_n^{-(a)}\big), \qquad v_n^{(b)} = \frac{1}{2Z_p^{(b)}}\big(w_n^{+(b)} - \mathcal{W}_n^{-(b)}\big). \tag{115}$$

Continuity of normal stress (36) and fault normal velocity (38) implies that these can be written as

$$\begin{bmatrix} \mathcal{W}_n^{-(a)} \\ \mathcal{W}_n^{-(b)} \end{bmatrix} = \frac{1}{Z_p^{(a)} + Z_p^{(b)}} \begin{bmatrix} Z_n^{(b)} - Z_p^{(a)} & 2Z_p^{(a)} \\ 2Z_p^{(b)} & Z_p^{(a)} - Z_p^{(b)} \end{bmatrix} \begin{bmatrix} w_n^{+(a)} \\ w_n^{+(b)} \end{bmatrix}. \tag{116}$$

All that remains is to show that (40) can also be written in characteristic form (35). We can write the shear stress and slip velocity using the characteristic variables (31):

$$\tau_m^{(a)} = \frac{1}{2}\big(w_m^{+(a)} + \mathcal{W}_m^{-(a)}\big), \qquad \tau_m^{(b)} = \frac{1}{2}\big(w_m^{+(b)} + \mathcal{W}_m^{-(b)}\big), \tag{117}$$

$$\tau_z^{(a)} = \frac{1}{2}\big(w_z^{+(a)} + \mathcal{W}_z^{-(a)}\big), \qquad \tau_z^{(b)} = \frac{1}{2}\big(w_z^{+(b)} + \mathcal{W}_z^{-(b)}\big), \tag{118}$$

$$v_m^{(a)} = \frac{1}{2Z_s^{(a)}}\big(w_m^{+(a)} - \mathcal{W}_m^{-(a)}\big), \qquad v_m^{(b)} = \frac{1}{2Z_s^{(b)}}\big(w_m^{+(b)} - \mathcal{W}_m^{-(b)}\big), \tag{119}$$

$$v_z^{(a)} = \frac{1}{2Z_s^{(a)}}\big(w_z^{+(a)} - \mathcal{W}_z^{-(a)}\big), \qquad v_z^{(b)} = \frac{1}{2Z_s^{(b)}}\big(w_z^{+(b)} - \mathcal{W}_z^{-(b)}\big). \tag{120}$$

Force balance (36) and the nonlinear friction law (40) then can be written as the nonlinear system

$$\mathbf{0} = \begin{bmatrix} \tau_m^{(a)} - \tau_m^{(b)} \\ \tau_z^{(a)} + \tau_z^{(b)} \\ \begin{bmatrix} \tau_m^{(a)} \\ \tau_z^{(a)} \end{bmatrix} - \begin{bmatrix} V_m \\ V_z \end{bmatrix} \frac{\sigma_n f(V,\psi)}{V} \end{bmatrix}, \qquad V = \sqrt{V_m^2 + V_z^2}, \tag{121}$$

where $V_m = -v_m^{(a)} - v_m^{(b)}$ and $V_z = -v_z^{(a)} + v_z^{(b)}$; see (39). The Jacobian of (121) with respect to the variables $\mathcal{W}_m^{-(a)}$, $\mathcal{W}_z^{-(a)}$, $\mathcal{W}_m^{-(b)}$, and $\mathcal{W}_z^{-(b)}$, is

$$\boldsymbol{J} = \frac{1}{2}\begin{bmatrix} 1 & 0 & -1 & 0 \\ 0 & 1 & 0 & 1 \\ 1 & 0 & 0 & 0 \\ 0 & 1 & 0 & 0 \end{bmatrix} + \frac{1}{2}\begin{bmatrix} \mathbf{0}_2 & \mathbf{0}_2 \\ \boldsymbol{J}_F^{(a)} & \boldsymbol{J}_F^{(a)} \end{bmatrix} \tag{122}$$

where $\mathbf{0}_2$ is the 2×2 zero matrix and

$$\boldsymbol{J}_F^{(a)} = \frac{1}{Z_s^{(a)}} \frac{\sigma}{V} \left(\begin{bmatrix} V_m^2 & V_m V_z \\ V_z V_m & V_z^2 \end{bmatrix} \frac{\frac{\partial f}{\partial V} V - f}{V^2} + \begin{bmatrix} f & 0 \\ 0 & f \end{bmatrix} \right), \tag{123}$$

$$\boldsymbol{J}_F^{(b)} = \frac{1}{Z_s^{(b)}} \frac{\sigma}{V} \left(\begin{bmatrix} V_m^2 & -V_m V_z \\ V_z V_m & -V_z^2 \end{bmatrix} \frac{\frac{\partial f}{\partial V} V - f}{V^2} + \begin{bmatrix} f & 0 \\ 0 & -f \end{bmatrix} \right), \tag{124}$$

with $f = f(V, \psi)$. The determinant of $\boldsymbol{J}$ is

$$J = \frac{1}{2V\tilde{Z}_s} (V\tilde{Z}_s + 2\sigma_n f) \left(\tilde{Z}_s + 2\sigma_n \frac{\partial f}{\partial V} \right). \tag{125}$$

If $\partial f / \partial V \geq 0$ then $J \neq 0$ and it follows by the implicit function theorem that friction law f is expressible in characteristic form.

References

1. Aagaard, B.T., Heaton, T.H., Hall, J.F.: Dynamic earthquake ruptures in the presence of lithostatic normal stresses: implications for friction models and heat production. Bull. Seismol. Soc. Am. **91**(6), 1765–1796 (2001). doi:10.1785/0120000257
2. Ampuero, J.-P.: Etude physique et numérique de la nucléation des séismes. PhD thesis, Univ. Denis Diderot, Paris (2002)
3. Andrews, D.J.: Rupture propagation with finite stress in antiplane strain. J. Geophys. Res. **81**(20), 3575–3582 (1976). doi:10.1029/JB081i020p03575
4. Andrews, D.J.: Dynamic plane-strain shear rupture with a slip-weakening friction law calculated by a boundary integral method. Bull. Seismol. Soc. Am. **75**(1), 1–21 (1985)
5. Aochi, H., Fukuyama, E., Matsu'ura, M.: Selectivity of spontaneous rupture propagation on a branched fault. Geophys. Res. Lett. **27**(22), 3635–3638 (2000). doi:10.1029/2000GL011560
6. Appelö, D., Petersson, N.A.: A stable finite difference method for the elastic wave equation on complex geometries with free surfaces. Commun. Comput. Phys. **5**(1), 84–107 (2009)
7. Appelö, D., Hagstrom, T., Kreiss, G.: Perfectly matched layers for hyperbolic systems: general formulation, well-posedness, and stability. SIAM J. Appl. Math. **67**(1), 1–23 (2006). doi:10.1137/050639107
8. Bayliss, A., Jordan, K.E., Lemesurier, B.J., Turkel, E.: A fourth-order accurate finite-difference scheme for the computation of elastic waves. Bull. Seismol. Soc. Am. **76**(4), 1115–1132 (1986)

9. Carpenter, M.H., Kennedy, C.A.: Fourth-order 2N-storage Runge-Kutta schemes. Technical report NASA TM-109112, National Aeronautics and Space Administration, Langley Research Center, Hampton, VA (1994)
10. Carpenter, M.H., Nordström, J., Gottlieb, D.: A stable and conservative interface treatment of arbitrary spatial accuracy. J. Comput. Phys. **148**(2), 341–365 (1999). doi:10.1006/jcph.1998.6114
11. Cruz-Atienza, V.M., Virieux, J.: Dynamic rupture simulation of non-planar faults with a finite-difference approach. Geophys. J. Int. **158**(3), 939–954 (2004). doi:10.1111/j.1365-246X.2004.02291.x
12. Das, S.: A numerical method for determination of source time functions for general three-dimensional rupture propagation. Geophys. J. R. Astron. Soc. **62**(3), 591–604 (1980). doi:10.1111/j.1365-246X.1980.tb02593.x
13. Das, S., Kostrov, B.V.: An investigation of the complexity of the earthquake source time function using dynamic faulting models. J. Geophys. Res. **93**(B7), 8035–8050 (1988). doi:10.1029/JB093iB07p08035
14. Day, S.M.: Three-dimensional finite difference simulation of fault dynamics: rectangular faults with fixed rupture velocity. Bull. Seismol. Soc. Am. **72**(3), 705–727 (1982)
15. Day, S.M., Dalguer, L.A., Lapusta, N., Liu, Y.: Comparison of finite difference and boundary integral solutions to three-dimensional spontaneous rupture. J. Geophys. Res. **110**, B12307 (2005). doi:10.1029/2005JB003813
16. de la Puente, J., Ampuero, J.-P., Käser, M.: Dynamic rupture modeling on unstructured meshes using a discontinuous Galerkin method. J. Geophys. Res. **114**, B10302 (2009). doi:10.1029/2008JB006271
17. Dunham, E.M., Belanger, D., Cong, L., Kozdon, J.E.: Earthquake ruptures with strongly rate-weakening friction and off-fault plasticity, Part 1: Planar faults. Bull. Seismol. Soc. Am. **101**(5), 2296–2307 (2011). doi:10.1785/0120100075
18. Dunham, E.M., Belanger, D., Cong, L., Kozdon, J.E.: Earthquake ruptures with strongly rate-weakening friction and off-fault plasticity, Part 2: Nonplanar faults. Bull. Seismol. Soc. Am. **101**(5), 2308–2322 (2011). doi:10.1785/0120100076
19. Festa, G., Vilotte, J.-P.: The Newmark scheme as velocity and stress time-staggering: an efficient PML implementation for spectral element simulations of elastodynamics. Geophys. J. Int. **161**(3), 789–812 (2005). doi:10.1111/j.1365-246X.2005.02601.x
20. Fornberg, B.: The pseudospectral method: accurate representation of interfaces in elastic wave calculations. Geophysics **53**(5), 625–637 (1988). doi:10.1190/1.1442497
21. Geubelle, P.H., Rice, J.R.: A spectral method for three-dimensional elastodynamic fracture problems. J. Mech. Phys. Solids **43**(11), 1791–1824 (1995). doi:10.1016/0022-5096(95)00043-I
22. Gustafsson, B.: The convergence rate for difference approximations to mixed initial boundary value problems. Math. Comput. **29**(130), 396–406 (1975)
23. Gustafsson, B., Kreiss, H.-O., Oliger, J.: Time Dependent Problems and Difference Methods. Wiley-Interscience, New York (1996)
24. Hagstrom, T., Mar-Or, A., Givoli, D.: High-order local absorbing conditions for the wave equation: extensions and improvements. J. Comput. Phys. **227**(6), 3322–3357 (2008). doi:10.1016/j.jcp.2007.11.040
25. Kame, N., Yamashita, T.: Simulation of the spontaneous growth of a dynamic crack without constraints on the crack tip path. Geophys. J. Int. **139**(2), 345–358 (1999). doi:10.1046/j.1365-246x.1999.00940.x
26. Kaneko, Y., Lapusta, N., Ampuero, J.-P.: Spectral element modeling of spontaneous earthquake rupture on rate and state faults: effect of velocity-strengthening friction at shallow depths. J. Geophys. Res. **113**, B09317 (2008). doi:10.1029/2007JB005553
27. Knupp, P.M., Steinberg, S.: The Fundamentals of Grid Generation. CRC Press, Boca Raton (1993)
28. Kozdon, J.E., Dunham, E.M.: Rupture to the trench in dynamic models of the Tohoku-Oki earthquake. Abstract U51B-0041 presented at 2011 Fall Meeting, AGU, San Francisco, Calif., 5–9 Dec., 2011
29. Kozdon, J.E., Dunham, E.M.: Rupture to the trench: dynamic rupture simulations of the 11 March 2011 Tohoku earthquake. Bull. Seism. Soc. Am. (2013, accepted). URL www.stanford.edu/~jkozdon/publications/kozdon_dunham_tohoku_BSSA12.pdf
30. Kozdon, J.E., Dunham, E.M., Nordström, J.: Interaction of waves with frictional interfaces using summation-by-parts difference operators: weak enforcement of nonlinear boundary conditions. J. Sci. Comput. **50**(2), 341–367 (2012). doi:10.1007/s10915-011-9485-3
31. Kreiss, H.-O.: Initial boundary value problems for hyperbolic systems. Commun. Pure Appl. Math. **23**(3), 277–298 (1970). doi:10.1002/cpa.3160230304
32. Kreiss, H.-O., Lorenz, J.: Intial-Boundary Value Problems and the Navier-Stokes Equations. Academic Press, New York (1989)
33. Kreiss, H.-O., Scherer, G.: Finite element and finite difference methods for hyperbolic partial differential equations. In: Mathematical Aspects of Finite Elements in Partial Differential Equations; Proceedings of the Symposium, Madison, WI, pp. 195–212 (1974)
34. Kreiss, H.-O., Scherer, G.: On the existence of energy estimates for difference approximations for hyperbolic systems. Technical report, Dept. of Scientific Computing, Uppsala University (1977)

35. Lapusta, N., Rice, J.R., Ben-Zion, Y., Zheng, G.: Elastodynamic analysis for slow tectonic loading with spontaneous rupture episodes on faults with rate- and state-dependent friction. J. Geophys. Res. **105**, 23765–23790 (2000). doi:10.1029/2000JB900250
36. Ma, S., Liu, P.: Modeling of the perfectly matched layer absorbing boundaries and intrinsic attenuation in explicit finite-element methods. Bull. Seismol. Soc. Am. **96**(5), 1779–1794 (2006). doi:10.1785/0120050219
37. Madariaga, R., Olsen, K., Archuleta, R.: Modeling dynamic rupture in a 3D earthquake fault model. Bull. Seismol. Soc. Am. **88**(5), 1182–1197 (1998)
38. Malvern, L.E.: Introduction to the Mechanics of a Continuous Medium, 1st edn. Prentice Hall, New York (1977)
39. Mattsson, K., Nordström, J.: Summation by parts operators for finite difference approximations of second derivatives. J. Comput. Phys. **199**(2), 503–540 (2004). doi:10.1016/j.jcp.2004.03.001
40. Miura, S., Takahashi, N., Nakanishi, A., Ito, A., Kodaira, S., Tsuru, T., Kaneda, Y.: Seismic velocity structure off Miyagi fore-arc region, Japan Trench, using ocean bottom seismographic data. In: Frontier Res. Earth Evolut., vol. 1, pp. 337–340 (2001)
41. Miura, S., Takahashi, N., Nakanishi, A., Tsuru, T., Kodaira, S., Kaneda, Y.: Structural characteristics off Miyagi forearc region, the Japan Trench seismogenic zone, deduced from a wide-angle reflection and refraction study. Tectonophysics **407**(3–4), 165–188 (2005). doi:10.1016/j.tecto.2005.08.001
42. Miyatake, T.: Numerical simulations of earthquake source process by a three-dimensional crack model. Part I. Rupture process. J. Phys. Earth **28**(6), 565–598 (1980)
43. Moczo, P., Kristek, J., Gallis, M., Pazak, P., Balazovjecha, M.: The finite-difference and finite-element modeling of seismic wave propagation and earthquake motion. Acta Phys. Slovaca **57**(2), 177–406 (2007)
44. Nilsson, S., Petersson, N.A., Sjogreen, B., Kreiss, H.-O.: Stable difference approximations for the elastic wave equation in second order formulation. SIAM J. Numer. Anal. **45**(5), 1902–1936 (2007). doi:10.1137/060663520
45. Noda, H., Dunham, E.M., Rice, J.R.: Earthquake ruptures with thermal weakening and the operation of major faults at low overall stress levels. J. Geophys. Res. **114**, B07302 (2009). doi:10.1029/2008JB006143
46. Nordström, J.: Conservative finite difference formulations, variable coefficients, energy estimates and artificial dissipation. J. Sci. Comput. **29**(3), 375–404 (2006). doi:10.1007/s10915-005-9013-4
47. Nordström, J., Carpenter, M.H.: High-order finite difference methods, multidimensional linear problems, and curvilinear coordinates. J. Comput. Phys. **173**(1), 149–174 (2001). doi:10.1006/jcph.2001.6864
48. Oglesby, D.D., Archuleta, R.J., Nielsen, S.B.: Earthquakes on dipping faults: the effects of broken symmetry. Science **280**(5366), 1055–1059 (1998). doi:10.1126/science.280.5366.1055
49. Olsson, P.: Summation by parts, projections, and stability. II. Math. Comput. **64**(212), 1473–1493 (1995)
50. Pelties, C., de la Puente, J., Ampuero, J.-P., Brietzke, G.B., Käser, M.: Three-dimensional dynamic rupture simulation with a high-order discontinuous Galerkin method on unstructured tetrahedral meshes. J. Geophys. Res. Solid Earth **117**, B02309 (2012). doi:10.1029/2011JB008857
51. Perrin, G., Rice, J.R., Zheng, G.: Self-healing slip pulse on a frictional surface. J. Mech. Phys. Solids **43**(9), 1461–1495 (1995). doi:10.1016/0022-5096(95)00036-I
52. Rice, J.R.: Constitutive relations for fault slip and earthquake instabilities. Pure Appl. Geophys. **121**(3), 443–475 (1983). doi:10.1007/BF02590151
53. Rice, J.R., Ruina, A.L.: Stability of steady frictional slipping. J. Appl. Mech. **50**(2), 343–349 (1983). doi:10.1115/1.3167042
54. Rice, J.R., Lapusta, N., Ranjith, K.: Rate and state dependent friction and the stability of sliding between elastically deformable solids. J. Mech. Phys. Solids **49**(9), 1865–1898 (2001). doi:10.1016/S0022-5096(01)00042-4
55. Roache, P.J.: Verification and Validation in Computational Science and Engineering. Hermosa Publishers, Albuquerque (1998)
56. Rojas, O., Dunham, E.M., Day, S.M., Dalguer, L.A., Castillo, J.E.: Finite difference modelling of rupture propagation with strong velocity-weakening friction. Geophys. J. Int. **179**, 1831–1858 (2009). doi:10.1111/j.1365-246X.2009.04387.x
57. Sato, M., Ishikawa, T., Ujihara, N., Yoshida, S., Fujita, M., Mochizuki, M., Asada, A.: Displacement above the hypocenter of the 2011 Tohoku-Oki earthquake. Science **332**(6036) (2011). doi:10.1126/science.1207401
58. Slaughter, W.S.: The Linearized Theory of Elasticity. Birkhäuser, Boston (2002)
59. Strand, B.: Summation by parts for finite difference approximations for d/dx. J. Comput. Phys. **110**(1), 47–67 (1994). doi:10.1006/jcph.1994.1005

60. Svärd, M., Nordström, J.: On the order of accuracy for difference approximations of initial-boundary value problems. J. Comput. Phys. **218**(1), 333–352 (2007). doi:10.1016/j.jcp.2006.02.014
61. Tessmer, E., Kosloff, D., Behle, A.: Elastic wave propagation simulation in the presence of surface topography. Geophys. J. Int. **108**(2), 621–632 (1992). doi:10.1111/j.1365-246X.1992.tb04641.x
62. Zhang, H., Chen, X.: Dynamic rupture process of the 1999 Chi-Chi, Taiwan, earthquake. Earth Sci. **22**(1), 3–12 (2009). doi:10.1007/s11589-009-0003-8